Estimation of surface soil moisture by a multi-elevation UAV-based ground penetrating radar

Qinbo Cheng[a*], Qiuju Su[a], Andrew Binley[b], Jintao liu[a], Zhicai Zhang[a], Xi Chen[c]

[a] State Key Laboratory of Hydrology-Water Resources and Hydraulic Engineering, Hohai University, Nanjing 210098, China

[b] Lancaster Environment Centre, Lancaster University, Lancaster, LA1 4YQ, UK

[c] Institute of Surface-Earth System Science, Tianjin University, Tianjin China

* Corresponding author: Qinbo.Cheng@hhu.edu.cn

Abstract: The measurement of soil moisture is important for a wide range of applications, including ecosystem conservation and agricultural management. However, most traditional measurement methods, e.g., time-domain reflectometry (TDR), are unsuitable for mapping field scale variability. In this study, we propose a method that uses an unmanned aerial vehicle (UAV) to support a ground penetrating radar (GPR) system for spatial scanning investigation at different elevations above ground level. This method measures the surface reflectivity to estimate the soil moisture, exploiting the linear relationship between the ratio of the reflected and the direct wave amplitudes along with the reciprocal of GPR antenna height. This relationship is deduced in this study based on the point source assumptions of a transmitter antenna and ground reflections, which is confirmed by numerical simulation results using the gprMax software. Unlike previous air-launched GPR methods, the UAV-GPR method presented here removes the limitations of a steady transmitter power and a fixed GPR survey height and the need for calibration of antenna transfer functions and geophysical inversion calculations, and thus is simpler and more convenient for field applications. We test the method at field sites within the riparian zone and a river-island grassland adjacent to the Yangtze River. The results from the field study illustrate comparable measured soil moisture to those obtained invasively using TDR. The root mean square error (RMSE) of surface reflectivity and soil moisture values between UAV-GPR with

8 antenna height investigations and TDR in the grassland are 0.03 and 0.05 cm^3/cm^3, respectively.

Keywords: UAV, GPR, reflectivity, permittivity, soil moisture.

1. Introduction

Surface soil water plays an important role in the exchange of energy and water. It provides valuable information for root zone water storage and soil water profile estimation [*Camillo and Schmugge*, 1983], and its measurement is considered to be the most basic index for irrigation management of crops [*Vereecken et al.*, 2008]. Measurement of surface soil water content is, therefore, important for ecosystem conservation and agricultural management [*Robinson et al.*, 2008], but also for assessing the surface boundary conditions for aquifer recharge processes.

In-situ soil moisture measurement methods (such as gravimetric analysis of samples, and volumetric sensing using time-domain reflectometry (TDR)) are widely used because of high measurement accuracy [*Stafford*, 1988]. However, these traditional measurement methods are invasive and have a relatively small measurement support volume, making them inefficient for assessing variation at the field (and larger) scale [*Robinson et al.*, 2008; *Wu et al.*, 2019].

Remote sensing technologies (such as microwave and optical satellites) provide effective tools for the regional ground soil moisture survey [*Karthikeyan et al.*, 2017a; b]. However, because of high elevation of remote sensing measurements, the spatial resolution of these methods is coarse, and the measurement accuracy is poor [*Lakshmi et al.*, 2013]. Recent developments in the relatively new ground-based cosmic-ray sensing method permits an assessment of soil moisture over relatively large areas, and offers great promise for monitoring large scale processes [*Andreasen et al.*, 2017]. However, there remains a need for mobile sensing approaches that can assess the variability of soil moisture at the field-scale.

Ground penetrating radar (GPR) is an effective tool for measuring soil moisture [*Babaeian et al.*, 2019; *Huisman et al.*, 2003; *Liu et al.*, 2019]. The basic principle of GPR is that a transmitting antenna emits a pulsed radar signal and a receiving antenna receives signals, either directly or reflected from contrasts in electrical properties in the soil profile [*Annan*, 2005; *Daniels*, 2004]. The velocity of the electromagnetic (EM) wave is inversely proportional to the dielectric permittivity, which is related to the water

content of the soil, as exploited in the conventional TDR measurement of soil moisture [*Anbazhagan et al.*, 2020; *Babaeian et al.*, 2019; *Huisman et al.*, 2003].

GPR can be used in a number of configurations for dielectric permittivity measurement. Adopting a common-offset configuration of transmitter (Tx) and receiver (Rx) antennas, signals reflected from depth in the soil can be used to assess EM wave velocity if the depth to the reflector (e.g., soil horizon) is known [*Lunt et al.*, 2005]. As this is often not the case, multi-offset methods, such as the common midpoint (CMP) or wide-angle reflection and refraction (WARR), offer an alternative, allowing the depth of a continuous reflector and the velocity of the EM wave reflected to be determined [*Huisman et al.*, 2003; *Kaufmann et al.*, 2020]. Such approaches are time consuming and offer low spatial resolution because of the need to change the Tx-Rx offset. In order to improve the measurement efficiency, multi-channel GPR systems have been utilized [*Kaufmann et al.*, 2020; *Muller*, 2020], although such systems are currently relatively expensive.

An alternative approach, using a common offset configuration, is to exploit signals observed from localized objects (such as stones) within the soil profile [*Daniels*, 2004; *Slater and Comas*, 2009]. The resultant hyperbolic patterns in the radargram can be analyzed easily to determine an effective EM wave velocity. However, such localized features are often not present, making such approaches somewhat limited.

Rather than measuring reflected waves, the direct wave (or "ground wave") offers information about the dielectric permittivity (and hence soil water content) at the ground surface [*Algeo et al.*, 2018]. Attempts have been made to utilize this for assessing variation in soil moisture, although analysis of such signals can be challenging.

Recognizing some of the challenges listed above for ground-based GPR measurement of soil moisture, air-launched approaches have been proposed [*Davis and Annan*, 2002; *Redman et al.*, 2002]. Such approaches exploit the fact that the amount of energy reflected at the air-soil interface is a function of the dielectric permittivity of the soil at the ground surface. For example, the surface reflectivity is expressed as the ratio of the reflected wave amplitude to the critical reference measurement above a perfect electric

conductor at a fixed survey elevation [*Davis and Annan*, 2002; *Redman et al.*, 2002]. However, for this surface reflection method, the requirements of a fixed survey elevation and a reference measurement increase the complexity of implementation and restrict its wide application [*Lambot et al.*, 2006a]. A full-wave inversion method based on the air-launched ultrawide band monostatic horn antenna has been used to estimate the soil moisture [*Lambot et al.*, 2004; *Dehem*, 2020; *Minet et al.*, 2012; *Wu et al.*, 2019]. However, results of this method greatly depend on the accuracy of observed signals affected by many factors (e.g., instrumental errors and environmental factors such as surface roughness and land cover) [*Andre et al.*, 2019; *Lambot et al.*, 2006b].

An airborne-mounted GPR provides a means of being able to distinguish the ground reflected wave from the air wave by increasing the travel time of ground reflected signals with increased elevation of the GPR antenna [*Diamanti and Annan*, 2017; *Edemsky et al.*, 2021]. Such an approach has an important advantage over earlier air-launched GPR by not requiring the operator ground access to the survey area, thus avoiding disturbance and land degradation, which could be important in sensitive or protected areas [*Edemsky et al.*, 2021; *Pritchard et al.*, 2020].

Airborne GPR with a helicopter or fixed-wing aircraft has shown promise in glaciology studies for assessing ice thickness [*Jenssen and Jacobsen*, 2021; *Pritchard et al.*, 2020]. Compared to piloted aircrafts, UAVs are more convenient, mobile, safe and affordable, and have become valuable remote sensing platforms [*Linna et al.*, 2022]. That said, we recognize that any airborne survey must be carried out within the constraints of local legislation. Modern UAVs are commonly equipped with accurate positioning strategies for flight trajectories that allow them to follow specified routes [*Catapano et al.*, 2021]. However, for the current-technology UAVs, there are still some limitations such as flight-time, load weight, etc.

One challenge of a UAV-GPR system is the source of in-flight magnetic and electromagnetic interference signals that are greater than the resolvability threshold of the GPR magnetometer. Fortunately, some studies indicate that the UAV-borne interference signal frequencies are much lower than the frequencies of GPR [*Walter et al.*, 2021]. Therefore, the electromagnetic interference generated by the UAV platform for GPR can be neglected. Note also, that the addition of a GPR transmitter to any

airborne platform may add further constraints on use, depending upon the local legal requirements for GPR use.

In recent years, there have been many applications for UAV-GPR systems including soil moisture mapping, and snow, ice, and glacier measurements [*Lopez et al.*, 2022; *Mangel et al.*, 2022; *Noviello et al.*, 2022]. *Lopez et al. [2022]* and *Noviello et al. [2022]* overviewed the technical solutions of UAV-based GPR systems and analyzed the main factors affecting performance, such as clutter waves, electromagnetic disturbances, flight stability and positional accuracy. *Mangel et al. [2022]* recently outlined some of the potential benefits and opportunities that UAV-based geophysical sensors offer for hydro-geophysical applications.

For soil moisture mapping, most studies have used the full-wave inversion method. For example, *Wu et al. [2019]* proposed a UAV-GPR with a lightweight hybrid horn-dipole antenna, and *Dehem [2020]* developed a UAV-GPR with a monostatic dipole antenna. However, the full-wave approach includes relatively complex processing steps, e.g., the antenna calibration and geophysical inversion. Furthermore, its measurement accuracy depends on the estimation of the antenna transfer functions and the stability of radar system [*Ardekani and Lambot*, 2014]. Our aim here is to propose and test a simple soil moisture estimation method with a UAV-GPR system that can be applied using widely available UAV and GPR instruments.

In this study, we utilize the DJI® T16 UAV (Shenzhen DJI Sciences and Technologies Ltd.) for a UAV-GPR system with the purpose of mapping shallow soil moisture. The theory of the reflection method for air-launched GPR is first developed, then we propose a multi-elevation UAV-GPR method to measure the ground reflectivity for the soil moisture estimation. We next test the method using a numerical model based on the gprMax software [*Warren et al.*, 2016] and field experiments. We then use the multi-elevation UAV-GPR method to measure the soil moisture distribution at two field sites and compare the measurement results with those measured by TDR. Finally, before offering some overall conclusions, we analyze and appraise various aspects of the method, including: the effect of antenna frequency; the benefit of obtaining measurements at multiple elevations; the measurement footprint and the possible effect of ground surface roughness.

2. Theoretical development

2.1 Relationship between reflected wave amplitude and GPR height

As stated earlier, GPR measurements are typically based on the transmission and reflection of a pulsed EM wave. This pulse is generated by a bow-tie transmitter antenna (Tx in Fig. 1a) in this study, reflected at medium boundaries where subsurface electrical properties change, and detected by the receiver antenna (Rx in Fig. 1a) [*Annan*, 2005; *Daniels*, 2004; *Travassos et al.*, 2018]. In addition to the reflected waves, Rx also receives the direct wave that travels directly between the transmitter and receiver antennas. If we consider an airborne antenna arrangement then we can ignore the effect of direct waves travelling along the ground surface. The direct wave is, therefore, simply the air wave, which arrives at Rx earlier than any reflected waves as its travel distance is shortest. As a result, the reflected wave at the ground surface is clearly separated from the direct wave [*Diamanti and Annan*, 2017], and amplitudes (i.e., signal) of the reflected and air waves can be separated easily (Fig. 1b).

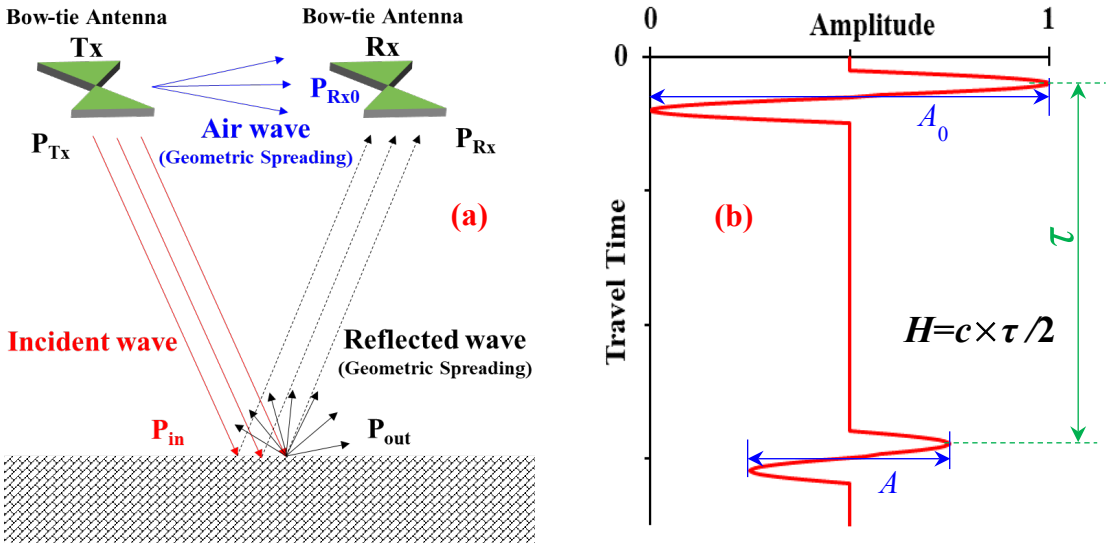

Fig. 1 Air-launched ground penetrating radar: (a) principle; (b) characteristic parameters of received radar signals, where A and A_0 are the amplitudes of reflected and air waves, respectively; H is the antenna height; τ is the travel time difference between reflected and air waves and c is the radar velocity in air ($\approx 3\times10^8$ m/s).

The EM wave from the bow-tie antenna will spherically spread in the air [*Annan*, 2005]. If we assume that the ground surface is an infinite plane, the ground surface will receive one half of the radar radiations:

$$P_{\mathrm{in}} = \frac{P_{\mathrm{Tx}}}{4\pi r^2} S = \frac{P_{\mathrm{Tx}}}{2}, \quad (1)$$

where P_{Tx} and P_{in} are the power of transmitter and incident waves, respectively; S is the received area at the ground surface; r is the distance from the transmitter.

When EM waves reach the ground surface, part of them will refract into the subsurface, and the remainder will reflect into the air. The power of reflected waves (P_{out}) is:

$$P_{\mathrm{out}} = \xi^2 P_{\mathrm{in}}, \quad (2)$$

where ξ is the reflectivity of the ground surface, and can be estimated as [*Ardekani*, 2013; *Huisman et al.*, 2003]:

$$\xi = -\frac{A_{\mathrm{out}}}{A_{\mathrm{in}}}, \quad (3)$$

where A_{in} and A_{out} are the amplitudes of incident and reflected waves on the ground, respectively.

Next, the reflected waves will spread spherically into the air, as shown in Fig. 1a. Because the effective reflected radar signals are from the first Fresnel zone that is proportional to the square root of antenna height [*Huisman et al.*, 2003], we can treat the ground surface as a point radar source, and then the power of reflected waves sensed by the receiver antennas can be estimated as:

$$P_{\mathrm{Rx}} = \frac{P_{\mathrm{out}}}{2\pi r^2} S_1 = \frac{\xi^2 P_{\mathrm{Tx}}}{4\pi H^2} S_1, \quad (4)$$

where P_{Rx} is the power of received reflected waves; S_1 is the received area of the receiver antenna; H is the height of the antenna.

The direct air waves arise from the geometric spreading of the radar (Fig. 1a). Thus, the power of air waves detected by receiver antennas can be expressed as:

$$P_{\mathrm{Rx0}} = \frac{P_{\mathrm{Tx}}}{S_2} S_1, \quad (5)$$

where P_{Rx0} is the power of received air waves; S_2 is the spreading area of radar from transmitter to receiver. If the transmitter can be treated as a point source, then S_2 is close to the spherical area：

$$S_2 \approx 4\pi D^2, \tag{6}$$

where D is the distance between transmitter and receiver.

Using Eqs. (4) and (5), we can write:

$$\frac{P_{\mathrm{Rx}}}{P_{\mathrm{Rx0}}} = \frac{\xi^2 S_2}{4\pi}\frac{1}{H^2}. \tag{7}$$

As the wave power is proportional to the square of the wave amplitude [*Annan*, 2005], we can translate Eq. (7) into:

$$\frac{P_{\mathrm{Rx}}}{P_{\mathrm{RX0}}} = \frac{aA^2}{aA_0^2} = \frac{A^2}{A_0^2} = \frac{\xi^2 S_2}{4\pi}\frac{1}{H^2}, \tag{8}$$

i.e.,

$$\frac{A}{A_0} = K\frac{1}{H}, \tag{9}$$

$$K = k \times |\xi|, \tag{10}$$

$$k = \sqrt{\frac{S_2}{4\pi}} \approx \sqrt{\frac{4\pi D^2}{4\pi}} = D, \tag{11}$$

where A and A_0 are the amplitudes of reflected and air waves, respectively; a is a constant; K is referred to as the ratio (i.e., slope coefficient) of A/A_0 to $1/H$; k is the GPR shape factor, which is related to the Tx-Rx separation distance (D), antenna directivity and antenna geometry. The value of k approximates D when the Tx antenna can be treated as a point source (Eq. (6)).

Eq. (9) shows that the amplitude of reflected wave (A) is inversely proportional to the GPR height (H). As shown in Fig. 1b, the amplitude values (i.e., A and A_0) can be directly extracted from received radar signals, and the antenna height (H) can be calculated by the travel time difference between the reflected and air waves. If we assume that the air wave amplitude (A_0) is constant (i.e., the power of transmitter

antenna is steady), the ratio of the ground reflected wave amplitude to the reflected wave amplitude above a metallic plate at a fixed GPR height is:

$$\frac{A}{A_0}\Big/\frac{A_\mathrm{m}}{A_0} = \left(\sqrt{\frac{S_2}{4\pi}}|\xi|\frac{1}{H}\right)\Big/\left(\sqrt{\frac{S_2}{4\pi}}|\xi_m|\frac{1}{H}\right) = \frac{|\xi|}{|-1|}, \quad (12)$$

i.e.,

$$|\xi| = \frac{A}{A_\mathrm{m}}, \quad (13)$$

where A_m is the amplitude of reflected wave measured over a metal plate target at a fixed elevation; ξ_m is the reflection coefficient of a metallic plate i.e., -1.

Eq. (13) is in agreement with the findings of *Redman et al.* [2002]. The deduction processes for Eq. (13), i.e., for previous air-launched GPR methods, rely on two assumptions: the transmitter power is always steady and the GPR height is fixed. However, in practice, these two assumptions are rarely satisfied, which may result in poor accuracy of measurements [*Huisman et al.*, 2003; *Lambot et al.*, 2006a; *Liu et al.*, 2019].

2.2 Principle of a multi-elevation UAV-GPR method

In consideration of GPR instrumental biases (i.e., the measurement errors of the reflected and direct wave amplitudes and the antenna height (Fig. 1b)), a multi-elevation investigation allows repeated measurement to reduce the effect of instrumental errors [*Schennach*, 2016]. We adopt the least squares approach to solve Eq. (9) for the change in the amplitude ratio with respect to the reciprocal of GPR height, i.e., the slope coefficient (K):

$$K = \frac{[\frac{1}{H_i}]\prime[\frac{A_i}{A_{0i}}]}{[\frac{1}{H_i}]\prime[\frac{1}{H_i}]} = \frac{\sum_1^n A_i/(A_{0i}H_i)}{\sum_1^n 1/H_i^2}, \quad (14)$$

where n is the number of measurements at a given horizontal position; H_i is the i_th GPR survey height; A_i/A_{0i} is the measurement of reflected and air wave amplitude ratio at the corresponding altitude of H_i.

Based on Eq. (14), we can solve Eq. (10) for surface reflectivity:

$$|\xi| = \frac{K}{k} = \frac{\sum_1^n A_i/(A_{0i}H_i)}{\sum_1^n 1/H_i^2}\frac{1}{k}. \quad (15)$$

In Eq. (15), the shape factor (k) can be calibrated based on Eq. (10) i.e., the linear relationship between the ratio of the reflected and air wave amplitude rate to the reciprocal of GPR height ($A/A_0 \sim 1/H$), and the corresponding surface reflectivity value (ξ). Based on the multi-elevation measurements above different ground surfaces with known surface reflectivity (e.g., a metallic plate or a water surface) we can use the least squares approach to solve Eq. (10) for the shape factor (k):

$$k = \frac{[|\xi_j|]'[K_j]}{[|\xi_j|]'[|\xi_j|]} = \frac{\sum_1^m |\xi_j| K_j}{\sum_1^m \xi_j^2}, \quad (16)$$

where m is the number of test points with different reflective materials; ξ_j and K_j are the known surface reflectivity and the estimated slope coefficient by the multi-elevation measurements (Eq. (14)) at the j_{th} measurement point, respectively.

As the radar antenna is pointing perpendicular to the ground surface, the relative dielectric permittivity (ε_r) can be computed using the surface reflectivity (ξ) [*Huisman et al.*, 2003]:

$$\varepsilon_r = \left(\frac{1+|\xi|}{1-|\xi|}\right)^2. \quad (17)$$

Based on the value of ε_r, the soil water content (θ) can be estimated by following, for example, the empirical equation for mineral soils [*Topp et al.*, 1980]:

$$\theta = -0.053 + 0.0291\varepsilon_r - 0.00055{\varepsilon_r}^2 + 0.0000043{\varepsilon_r}^3. \quad (18)$$

In summary, based on the multi-elevation measurements (i.e., Eq. (14)), Eq. (16) provides a means of calibrating the shape factor (k) of the GPR using survey results over different test materials with known surface reflectivity, and Eqs. (15), (17) and (18) form a method to estimate the surface reflectivity (ξ), permittivity (ε_r) and soil moisture (θ), respectively, at investigation points.

Many previous studies have found that the moisture sampling depth of air-launched GPR (i.e., microwave emission) depends on a number of factors such as radar frequency, soil features (e.g., soil texture, moisture and density), and soil horizontal layering [*Wu and Lambot*, 2022; *Lambot et al.*, 2006a; *Minet et al.*, 2010]. However, there is no widely accepted (microwave radiative transfer) model for predicting the moisture sampling depth at different radar frequencies [*Shen et al.*, 2020]. Many studies, based on theoretical and experimental analyses, have indicated that the sampling depth for the L-band (1–2 GHz/30–15 cm wavelength) radiometry is about 5 cm, and 10 cm for P-band (0.3–1 GHz/100–30 cm wavelength) radiometry [*Shen et al.*, 2020; *Boopathi et al.*, 2018; *Escorihuela et al.*, 2010; *Ye et al.*, 2020; *Yueh et al.*, 2019; *Zheng et al.*, 2019].

3. Experimental methodology

We first outline our methodology for using numerical simulations to test the multi-elevation UAV-GPR system and then describe the field-based deployment at two study sites.

3.1 Numerical simulation

Numerical models can be used to simulate the propagation of EM waves and thus can be useful to assess the theoretical characteristics of a GPR system. In this study, we utilize the gprMax software [*Warren et al.*, 2016], which solves Maxwell's equations in three dimensions using the finite difference method. A two-layer (i.e., free space and ground) numerical model was built to simulate the effects of different ground materials and GPR heights on the signals of a GPR antenna arrangement as shown in Fig. 1a. In our numerical model, the simulated spatial domain is 0.80 m (length) × 0.80 m (width) × 2.5 m (height). The vertical dimension is split into two layers: an upper layer of 2.3 m thickness representing free space, and a 0.2 m thick lower layer representing the studied (soil) medium. The spatial and temporal discretization are set to 0.001 m and 0.002 ns, respectively. A built-in GPR antenna module (i.e., "Mala 1.2GHz") is used to model the features of antennas similar to commercial GPR antennas.

In order to analyze the relationship between the amplitude of reflected wave (A) and

GPR antenna height (H) (i.e., Eq. (9)), and between the slope coefficient (K) and the dielectric permittivity (ε_r) of ground material (i.e., Eq. (10)), we considered several modeling scenarios. First, we fixed the dielectric permittivity of the ground material, and ran the numerical model with different GPR heights (specifically, H ranging from 0.3 to 0.8 m with an interval of 0.05 m and from 0.4 to 2.0 m with an interval of 0.4 m in order to balance the range of simulated GPR heights and computational efficiency). Then we repeated the process using a different dielectric permittivity of the lower unit. In our case, we consider a relative permittivity of 2, 5.4 and 16, and a metal material with very high relative permittivity in order to uniformly cover the range of surface absolute reflectivity (i.e., from 0 to 1). In each modeling scenario, the amplitudes of the air and reflected waves are recorded to estimate their ratio (Eq. (9)).

3.2 Field test

In this study, a 7.85 kg 250 MHz shielded antenna (with an effective sampling depth of 0.12 m [*Wang*, 1987]) from Mala® was suspended from a DJI® T16 UAV by two ropes each with 15 m in length (in order to avoid mutual interference between UAV and GPR) as shown in Fig. 2. The GPR controller, which communicates with the antenna by a fiber optic cable, was also attached to the UAV (Fig. 2), and employs a time-triggered measurement method. The UAV used was selected because of its high-accuracy positioning system (i.e., the real-time kinematic positioning technique (RTK), where the horizontal and vertical positional accuracies are all $\pm$0.1 m), a maximum loading capacity of 16 kg and hovering time of about 10 - 18 minutes. The remote controller of the UAV allows the operator to plan the flight route and survey height.

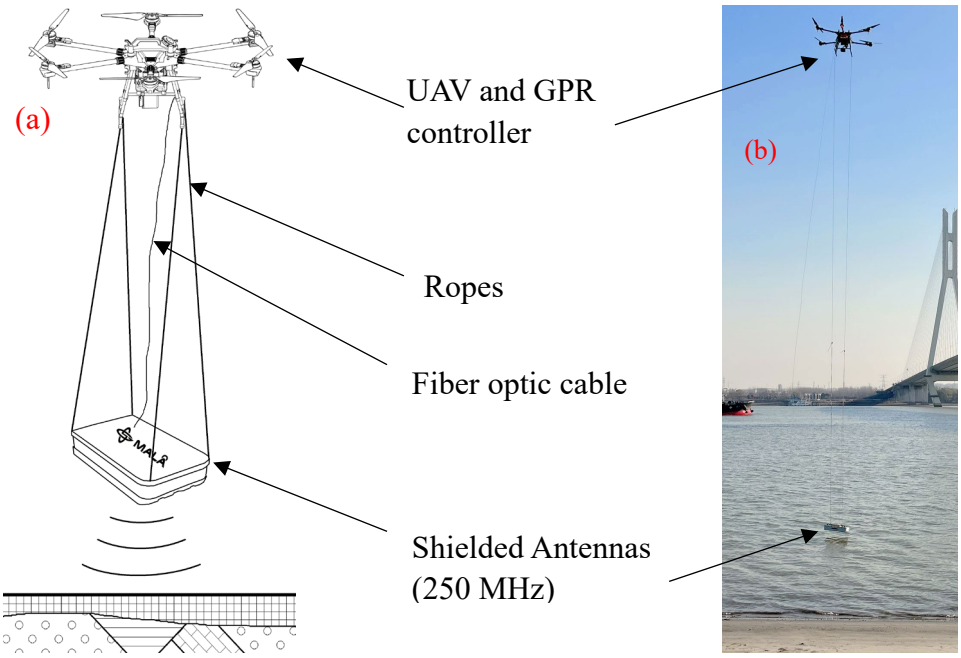

Fig. 2 Multi-elevation GPR carried by UAV: (a) sketch of configuration; (b) prototype system in operation above a water surface (of known reflectivity).

As the GPR is static to the UAV in the UAV-GPR system, the difference between the antenna height measured by GPR (Fig. 1b) and the UAV elevation collected by RTK is constant at a measurement point. Therefore, we can align the GPR measurement time to the UAV system time by matching the time series of antenna heights measured by GPR with that of UAV elevations collected by RTK according to their texture features for the time registration of GPR measurements. And then based on the corrected GPR measurement time, the position information of UAV is assigned to GPR measurements using a linear interpolation.

For the UAV-GPR system in this study, there are two measurement modes: point and route. For the point measurement mode, the UAV slowly raises the GPR antenna vertically, allowing GPR measurements at different antenna heights (in our case from 0 to 15 m). In order to reduce the effect of instrumental errors, repeated measurements by multiple (UAV) take-off and landing can be used. In the route measurement mode, the UAV carries the antenna along the planned flight route at pre-defined heights. The route measurement method, therefore, permits mapping at the field scale. We test the

UAV-GPR method at two field sites within the riparian transect and the river-island grassland adjacent to the Yangtze River (Fig. 3a).

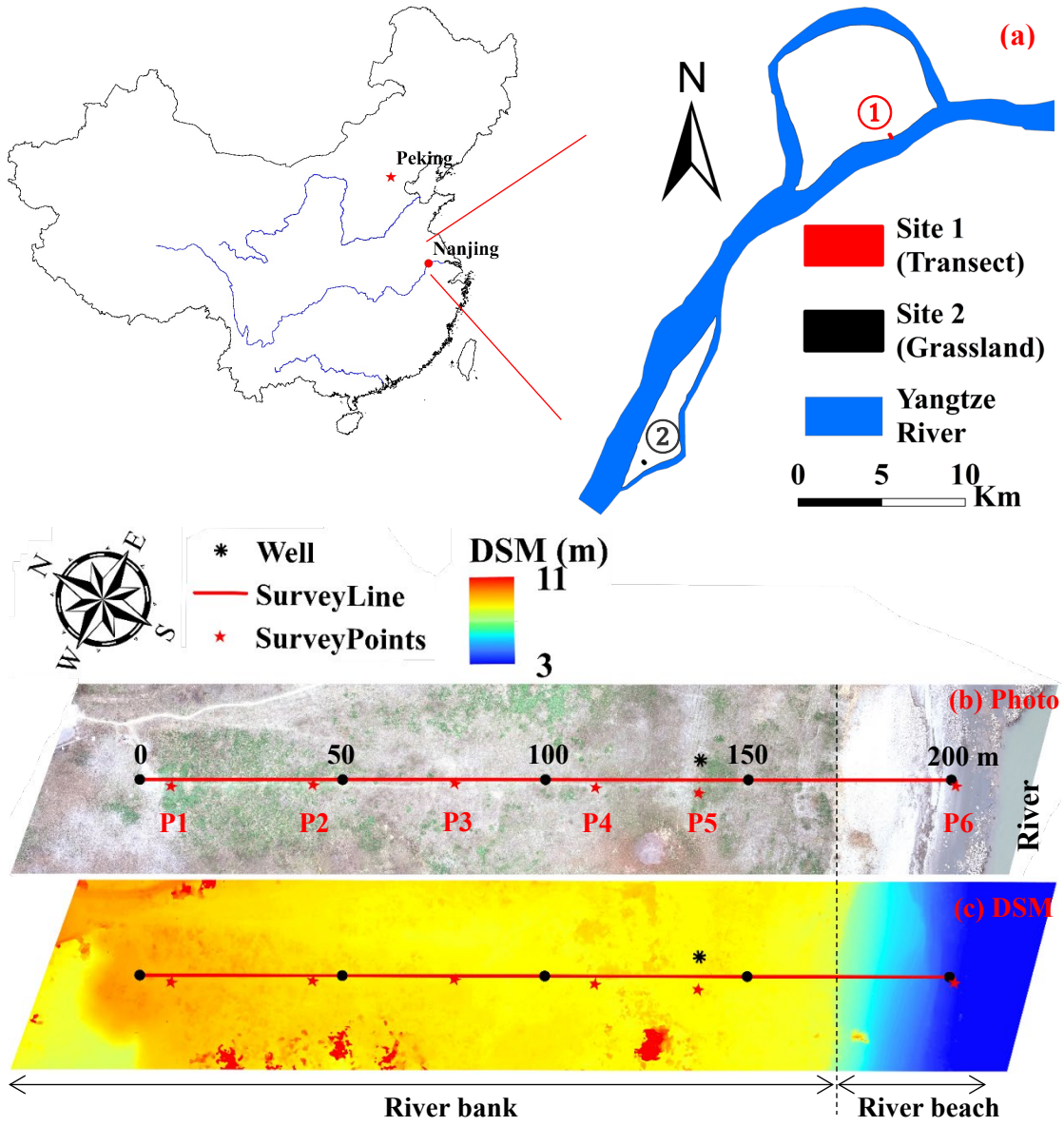

Fig. 3 Location and geographic features of the riparian transect: (a) location; (b) aerial orthophoto; (c) digital surface model. Six red star symbols (P1 to P6) indicate locations where the point method was applied. The black asterisk marks the location of an observation well. The red line presents the route survey line, and the black circular symbols show the map scale.

(1) Field Site 1: Riparian Transect

One field test area is a 200 m transect located in the riparian zone of the Yangtze River

388 in Nanjing, China (Fig. 3a). The test area belongs to the flood plain of Yangtze River,
389 where the main soil type is loamy sand. On Jan 3, 2022, we used the UAV to take aerial
390 photos in this area, then we used the DJI Terra software to generate an orthophoto (Fig.
391 3b) and a digital surface model (DSM, Fig. 3c). Fig. 3 shows some vegetation (e.g.,
392 Wormwood and Setaria) within the study area, and relatively flat topography. The
393 topography at the river beach close to the Yangtse River is relatively steep, and
394 vegetation cover is absent. Observations of water level in a groundwater monitoring
395 well within the study (black asterisk in Fig. 3b) revealed a depth to the water table of
396 3.15 m. The electric conductivity and temperature in the Yangtze river (at the time of
397 surveying) were about 35 mS/m and 13 °C, respectively.
398
399 The Mala GPR 250 MHz shielded antenna was selected for testing the methodology
400 (see Fig. 2). In order to estimate the shape factor (k) of the GPR, we chose six points
401 (indicated in Fig. 3b) along the survey line to carry out measurements at a range of
402 elevations, i.e., the point method detailed earlier. As the specific EM features (i.e., high
403 reflection) of water and metal bodies are known, we also tested the UAV-GPR system
404 over the water surface (Fig. 2b at the Yangtse River) and an iron plate (6 m (length) ×
405 6 m (width) × 0.01 m (thickness)) placed on the ground surface.
406
407 For testing the capacity of UAV-GPR in spatial scanning (i.e., the 'route' method
408 outlined earlier), the UAV-GPR system was flown along the survey line (shown in Fig.
409 3b) at a fixed elevation to investigate the reflectivity of ground surface. In order to
410 improve the measurement accuracy, we repeated the survey with different elevations,
411 giving observations with antenna heights of 5, 10 and 15 m above ground level.
412
413 For comparison purposes, we measured the relative permittivity (and soil moisture)
414 using the TDR with 0.1 m probe length from Acclima®. From the measured relative
415 permittivity (ε_r), the reflectivity (ζ) at the ground surface can also be computed, which
416 is the inverse of Eq. (17):

$$|\xi| = \left|\frac{1-\sqrt{\varepsilon_r}}{1+\sqrt{\varepsilon_r}}\right|. \quad (19)$$

In this study the TDR measurements conducted at 0-10 cm depth might represent almost similar sampling depth as the ones for UAV-GPR employing 250 MHz antenna [*Shen et al.*, 2020; *Wang*, 1987]. These measurements were made at the ground surface with the interval of 0.5 m along the transect. The root mean square error (RMSE) was used to compare the GPR results with the TDR measurements in the center of the first Fresnel zone under the assumption of the relatively uniform surface reflectivity:

$$RMSE = \sqrt{\frac{1}{L}\sum_{i=1}^{L}(y_{\mathrm{GPR},i} - y_{\mathrm{TDR},i})^2}, \quad (20)$$

where L is the number of measurements, and $y_{\mathrm{GPR},i}$ and $y_{\mathrm{TDR},i}$ are the i_{th} measurement of GPR and TDR, respectively.

(2) Field Site 2: Grassland

In order to test the UAV-GPR method further, a small grassland located in a river island in the Yangtze River in Nanjing, China (Fig. 3a) was investigated. The grassland area is about 3, 000 m^2, and the main soil type is loam. The orthophoto (Fig. 4a) and the digital surface model (DSM, Fig. 4b) of the test area were produced from surveys with a DJI phantom UAV. As shown in Fig. 4, a water filled channel is included to test the capability of water surface detection by the UAV-GPR. Fig. 4a presents that in this study area, the vegetation coverage is heterogenous, and weed coverage in the middle area is denser than that in other zones. This may suggest that the soil moisture distribution is uneven, and the soil in the center area is moister. In the southeast boundary, there are two small drainage ditches that are perpendicular to each other (see blue lines in Fig. 4a), the width and depth of which are about 1.4 and 0.25 m, respectively. These drainage features will affect the local surface soil roughness as they clearly increase the surface protuberance or depression [*Lambot et al.*, 2006b].

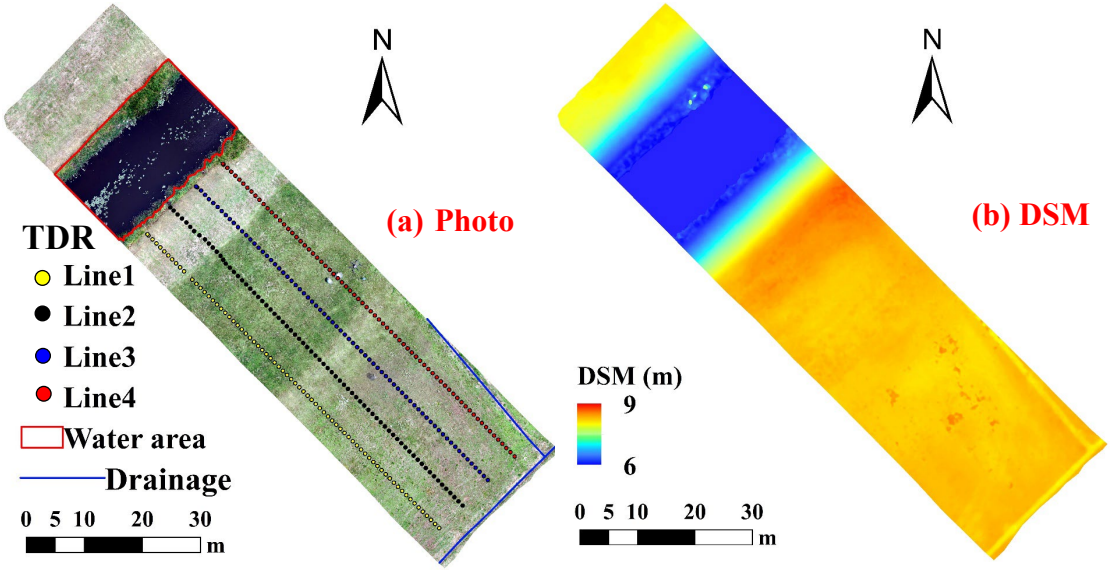

Fig. 4 Geographic features of the grassland: (a) aerial orthophoto; (b) digital surface model. The water filled channel is demarked by a red line. The TDR survey lines are numbered as 1, 2, 3 and 4 sequentially from left to right.

In the test area, we programmed 14 parallel flight routes with the spacing of 2 m, which are perpendicular to the channel. The flight velocity was set to 2.0 m/s, and the time interval of GPR records was 0.1 s. In order to reduce the effect of GPR instrumental biases (Fig. 1b), we repeated the survey with 8 antenna heights above ground level, i.e., 2.0, 2.5, 3.0, 3.5, 4.5, 5.5, 6.5 and 8.5 m. Along selected four flight routes (Fig. 4a) with a spacing of 6 m, we measured the soil relative permittivity (and thus soil moisture) using the TDR from Acclima® at 1 m intervals to compare against the GPR measurements.

4. Results

4.1 Numerical experiments of multi-elevation GPR

The results of the two-layer numerical modeling showing the ratios of the ground-surface reflected and the air wave amplitudes (A/A_0) at different heights (H) are presented in Fig. 5a. The figure indicates that for all cases with different dielectric permittivity (ε_r) values, the ratio of ground-surface reflected to air wave amplitudes

significantly linearly varies with the reciprocal value of GPR height. This linear relationship is in agreement with Eq. (9). Fig. 5a also shows that the slope coefficient (K) of the trend line between the amplitude ratio and the reciprocal of GPR height clearly increases with the relative dielectric constant (ε_r) of material representing ground surface conditions.

In Fig. 5b, we plot the slope coefficient (K) of trend lines in Fig. 5a versus the absolute reflectivity ($|\xi|$) of materials, where ξ is calculated by the dielectric constant (Eq. (19)). For the metallic material, the absolute reflectivity value is 1.0 as it can be treated as the perfect electric conductor [*Redman et al.*, 2002]. Fig. 5b shows that there is a clear linear relationship between the slope coefficients (K) and the absolute reflectivity values ($|\xi|$), which is consistent with Eq. (10). According to Eq. (16), we can calculate the shape factor (k) (i.e., 0.081 m) for the Mala GPR with a 1.2 GHz shielded antenna. The estimated value of k is close to the distance (i.e., 0.076 m) between transmitter and receiver antennas, which is consistent with Eq. (11).

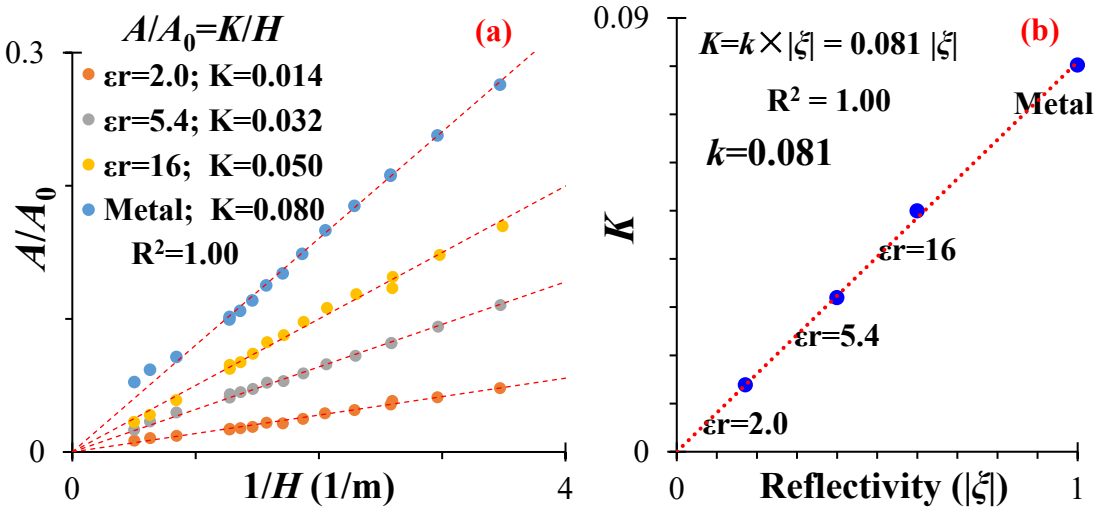

Fig. 5 Numerical simulation results: (a) the reflected and air wave amplitude ratio (A/A_0) versus the reciprocal of GPR height ($1/H$); (b) the slope coefficient (K) of trend line in Fig. 5a versus the absolute reflectivity ($|\xi|$) of ground surface. The dashed lines are the linear trend lines with an intercept of 0. The symbols with different colors represent the different materials considered.

In summary, the results of the numerical simulation confirm, theoretically, the two linear relationships in Eqs. (9-10) inferred from the theoretical development of the method, and support that the shape factor (k in Eq. (11)) is close to the Tx-Rx antenna separation distance.

4.2 Field experiments of multi-elevation GPR

4.2.1 Point measurement mode for calibration and validation of the UAV-GPR method

As described earlier, in order to implement the multi-elevation measurements in the point measurement mode, the UAV lifts up/down the GPR antenna vertically (with a velocity of 0.1 m/s), and the GPR system continuously records data with the interval of 0.2 s. The field investigation results of the UAV-GPR system with the point measurement mode at the six points (i.e., at the positions marked with red stars in Fig. 3b), the Yangtze River surface and the iron plate are shown in Fig. 6. This figure shows that at each survey point, there is a clearly linear relationship between the reflected and air wave amplitude ratios (A/A_0) and the reciprocal values of GPR heights ($1/H$), which confirms the result of Eq. (9) inferred in this study. The slope coefficient (K) of trend line between the reflected and air wave amplitude ratio and the reciprocal of GPR height varies with the studied medium.

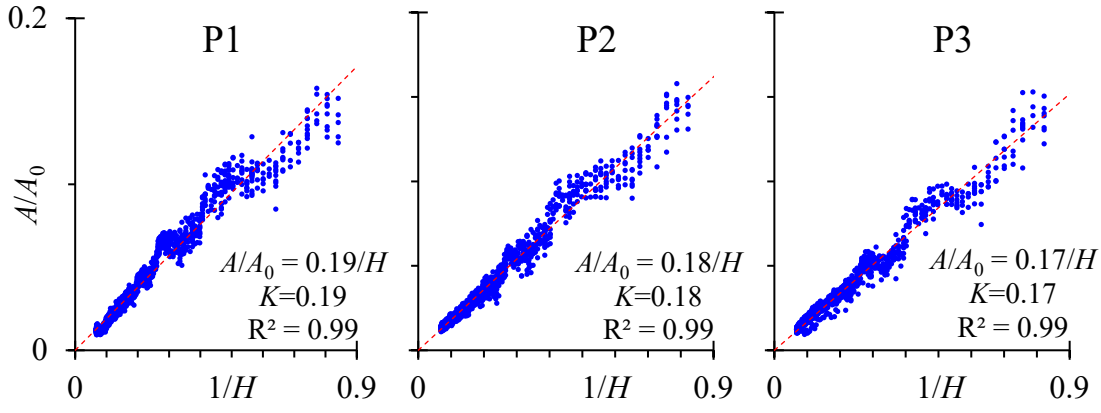

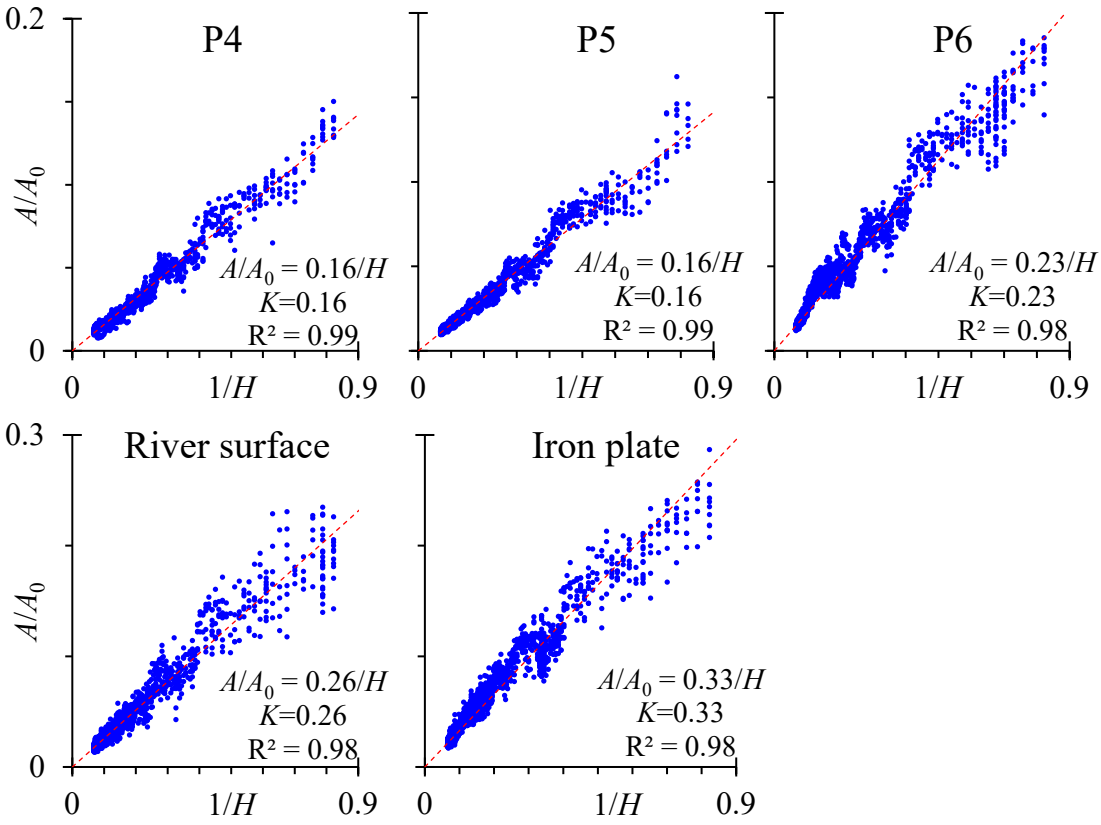

Fig. 6 The ratio of the reflected to air wave amplitudes (A/A_0) versus the reciprocal of GPR height ($1/H$) at the six test points, the river surface and the iron plate. The red dashed lines are the linear trend lines with an intercept of 0.

The slope coefficient (K) of linear trend line (in Fig. 6) versus the absolute reflectivity ($|\zeta|$) of ground surface for different survey points is presented in Fig. 7. In this figure, the reflectivity values are calculated by Eq. (19) according to the TDR measured relative dielectric constant (ε_r) values of soils at the six survey points and known values for water (Yangtze River site) and metal (iron plate). This figure shows that the slope value (K) clearly varies linearly with the material reflectivity, which is in agreement with Eq. (10). Based on Eq. (16), we can calculate the shape factor (k) for Mala 250 MHz shielded antenna as 0.33 m. The estimated value of k is close to the Tx-Rx separation distance of 250 MHz shielded antenna (i.e., 0.31 m), which is in line with Eq. (11).

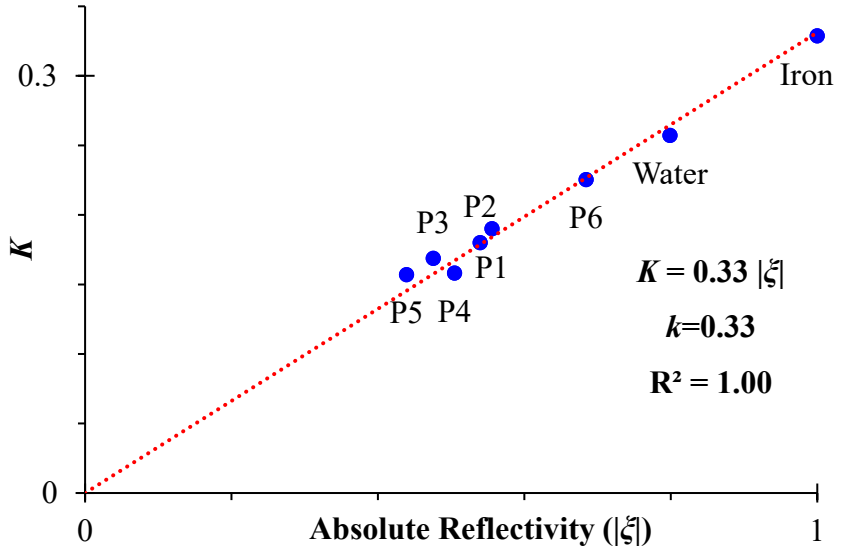

Fig. 7 The slope coefficient (K) of trend line between the reflected and air wave amplitude ratio and the reciprocal of GPR height (in Fig. 6) versus the absolute reflectivity ($|\xi|$) of ground surface. The red dashed line is the linear trend line with the intercept of 0.

In summary, similar to the numerical simulation results, the field point experiments also support the underlying theory of surface reflectivity detection (Eqs. (9)-(11)) by the multi-elevation UAV-GPR method, and allow the calculation of the shape factor (k) of the Mala 250 MHz shielded antenna for surface reflectivity estimation (Eq. (15)).

4.2.2 Route measurement mode for spatial scanning investigations

(1) Field Site 1: Riparian Transect

The results of UAV-GPR measurement along the survey line (i.e., red line in Fig. 3b) at three different elevations (i.e., 5, 10 and 15 m) are shown in Fig. 8. This figure shows that the travel time of surface reflected wave clearly increases with the GPR height, and at the higher GPR altitude, the separation of reflected and air waves is more obvious. The different brightness of the GPR images (i.e., the GPR receiving signal values) for three survey elevations possibly results from the unsteady power (i.e., A_0 or P_{Tx} in Fig. 1) of the Tx antenna.

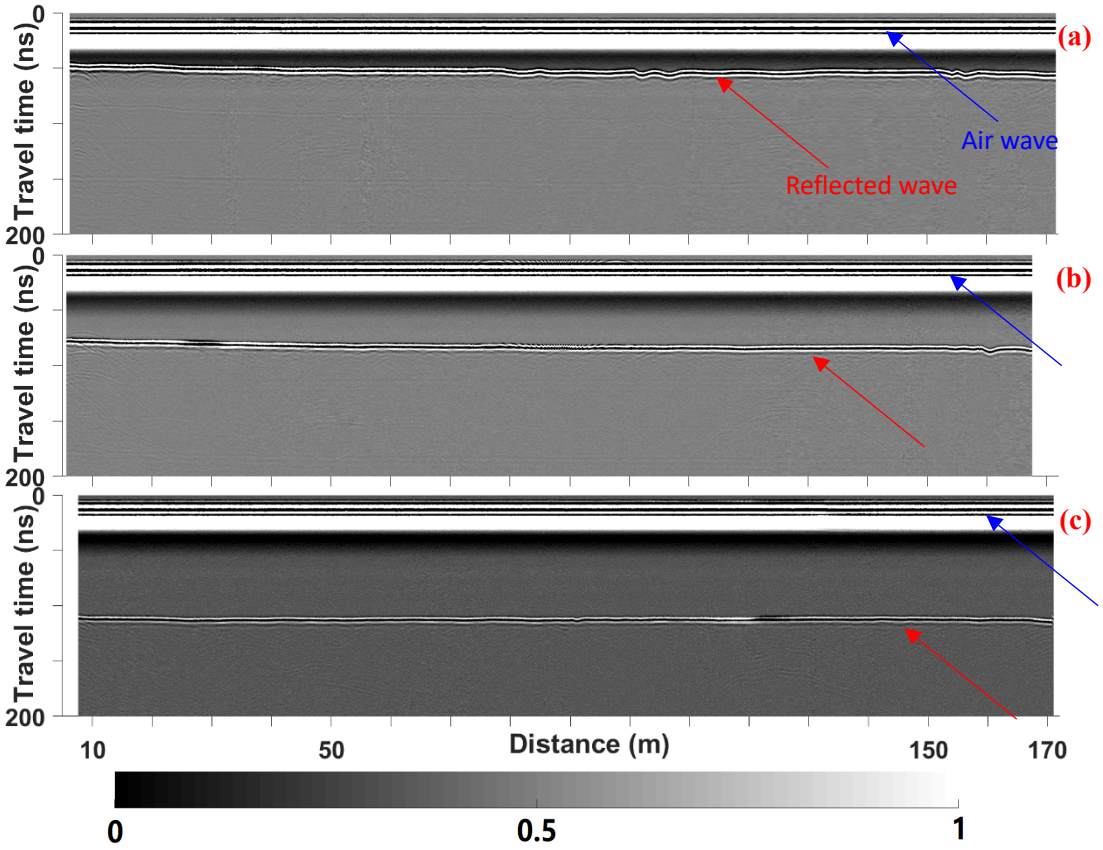

Fig. 8 Normalized raw GPR signals received along the survey line at different antenna elevations: (a) 5 m; (b) 10 m; and (c) 15 m.

According to Eqs. (15), (17) and (18), the surface reflectivity (ξ), relative dielectric permittivity (ε_r) and soil moisture (θ) are estimated along the survey line based on the reflected and air wave amplitude ratio and the corresponding GPR height as shown in Fig. 9. In this figure, the surface reflectivity is estimated by Eq. (19) using the relative permittivity measured by TDR, and the black line presents the smooth value of UAV-GPR measurements using the moving average filter with the span of 2 m. Compared with the smoothed values, there is some apparent bias in the UAV-GPR measurements, which possibly originates from the instrumental errors (Fig. 1b) of the GPR and the different sampling volumes between TDR and GPR. The variations in inferred properties from both UAV-GPR and TDR along the survey line are large: the coefficients of variation are generally greater than 10%. This represents the high heterogeneity of soil moisture at the ground surface affected by land cover and variation in soils. Fig. 9 also points out that the trend of GPR measurements along the transect matches, in general, that of the TDR measurements. When TDR measurement is high then GPR measurement is generally high, and vice versa.

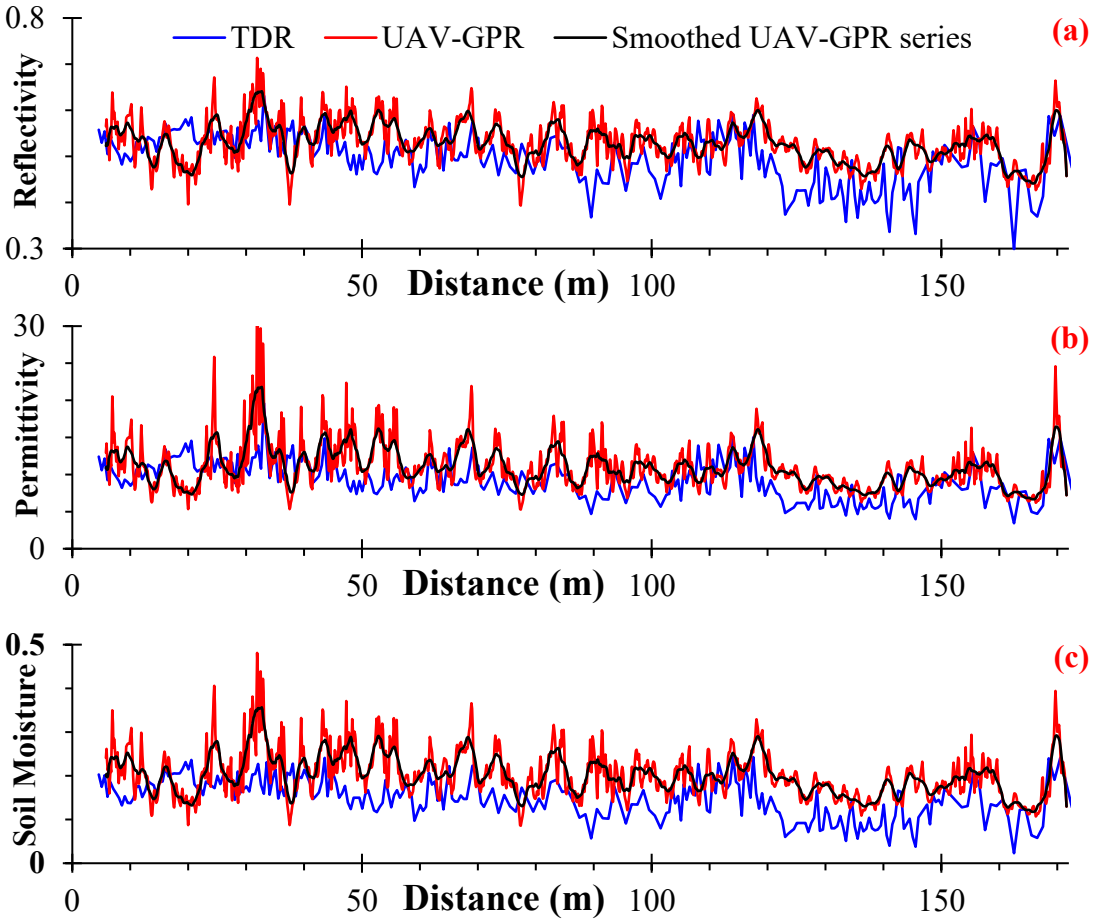

Fig. 9 Comparison of the UAV-GPR and TDR measurement results along the survey line: (a) absolute reflectivity; (b) relative permittivity; (c) soil moisture.

The measurements of UAV-GPR and TDR are compared in Fig. 10. In this figure, most points scatter around the 1:1 line. The RMSE values of reflectivity, permittivity and soil moisture are 0.065, 3.5 and 0.075 cm^3/cm^3, respectively. The relative error of mean reflectivity between TDR and GPR is less than 10%. In contrast, the greater mismatch of permittivity may result from the error magnification effect by Eq. (17). Errors in the assumed universal relationship between permittivity and soil moisture content (Eq. (18)) may also contribute to some differences between GPR and TDR inferred soil moisture values. The GPR measured values of reflectivity (and so permittivity and soil moisture) are generally higher than those for the TDR (Fig. 10), which may be caused by the effect of land cover (Fig. 3b). Note also that the TDR and GPR measurements have different support volumes (measurement footprint). In our analysis we have compared

583 a single TDR measurement in the center of the GPR footprint; variation of TDR-scale
584 measurements within this footprint may contribute to the difference between to the two
585 data types.
586

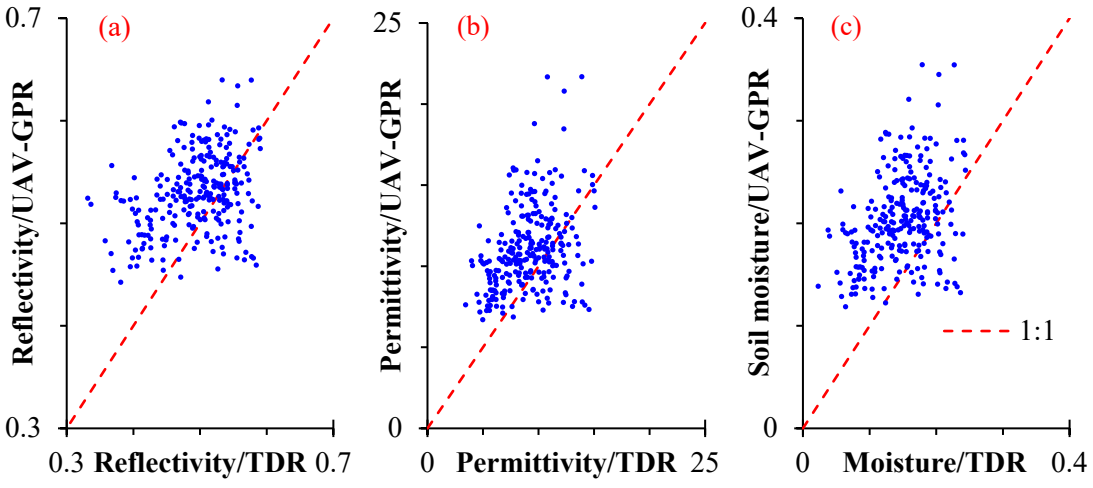

587
588 Fig. 10 UAV-GPR results versus TDR measurements: (a) absolute reflectivity; (b)
589 relative permittivity; (c) soil moisture. The red dashed line indicates a 1:1 match.
590
591 *(2) Field Site 2: Grassland*
592 Based on the GPR measurements at eight antenna heights, the surface absolute
593 reflectivity values at investigation points (Fig. 11a) can be calculated by Eq. (15). The
594 spatial distribution of surface reflectivity (Fig. 11b) is estimated from GPR point
595 measurement results (Fig. 11a) using interpolation by kriging. The permittivity (Fig.
596 11c) and moisture (Fig. 11d) are computed by, respectively, Eqs. (17) and (18) based
597 on the estimated surface reflectivity. Fig. 11b shows the high reflectivity area (i.e., red
598 area) matches, in general, with the water-covered area extracted from the orthophoto
599 (Fig. 4a). It confirms the detection ability of the UAV-GPR method. In Fig. 11, the
600 extremely low or high values in the southeast boundary possibly result from the effect
601 of drainage (Fig. 4), because the drainage ditches, with a depth of 0.25 m, obviously
602 increase the surface protuberance, and thus affect the local surface soil roughness
603 [*Lambot et al.*, 2006b].
604

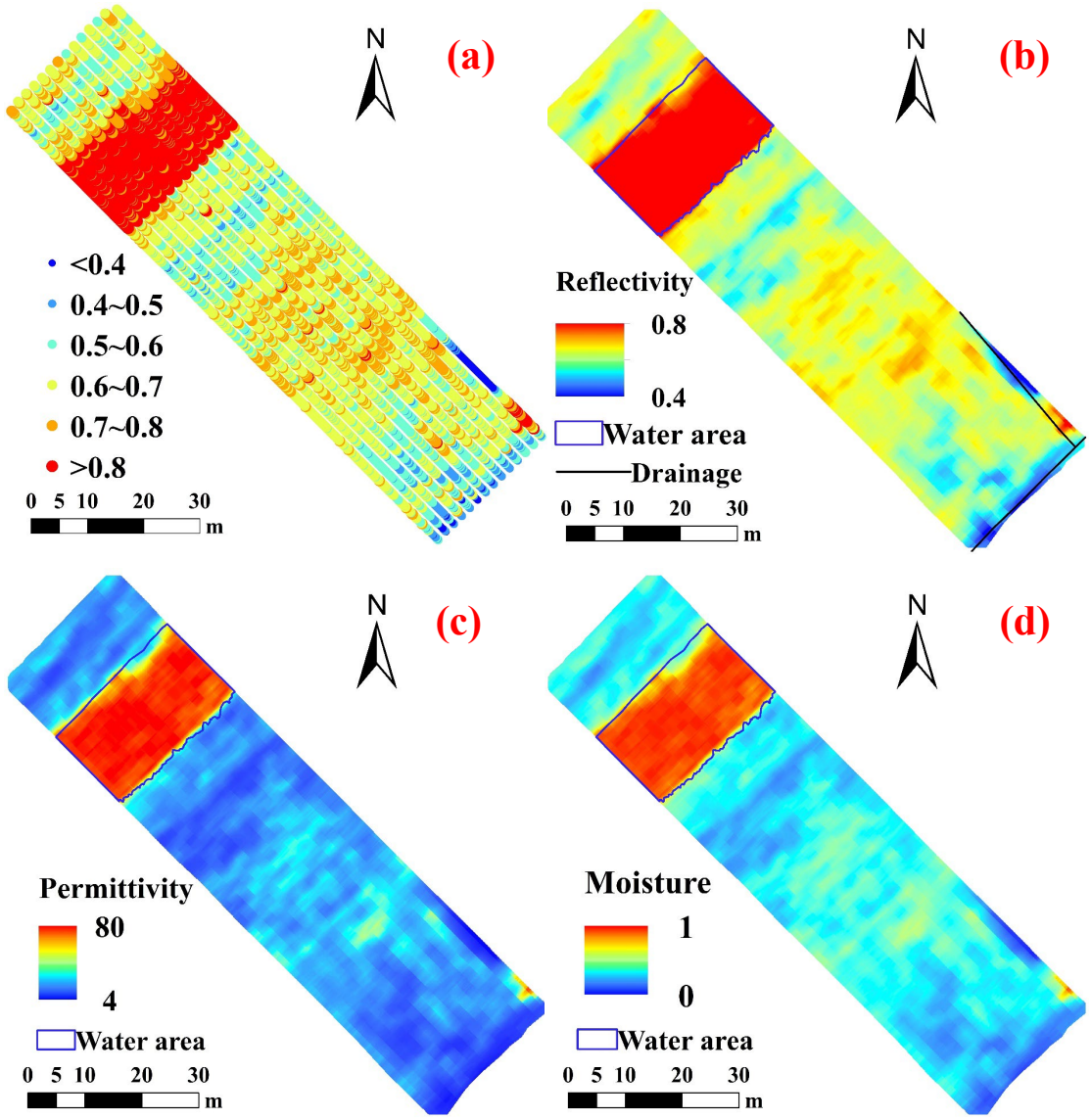

Fig. 11 Measurement results of UAV-GPR in the grassland area: (a) surface absolute reflectivity at measurement points; (b) spatial distribution of surface absolute reflectivity interpolated by Kriging; (c) permittivity; (d) soil moisture.

In Fig. 12, we compare the surface reflection measured by UAV-GPR with that estimated by Eq. (19) using permittivity measured by TDR. This figure shows that the GPR measurements generally match with the TDR estimations, and the trend of surface reflectivity values along the survey lines are similar. The measurements of GPR and TDR for four survey lines (see Fig. 4a for location) are compared in Fig. 13. In this figure, most points scatter around the 1:1 line. The RMSE of surface reflectivity,

relative permittivity and soil moisture values between GPR and TDR are 0.033, 4.1, and 0.050, respectively. The mismatches between GPR and TDR in the grassland are generally less than that in the riparian transect (Field Site 1) possibly because in the grassland, there are more investigation heights of UAV-GPR, the vegetation is sparser and shorter, and the soil is moister. The wetter soil enhances contact between TDR probes and soils, and thus improves the measurement accuracy of TDR.

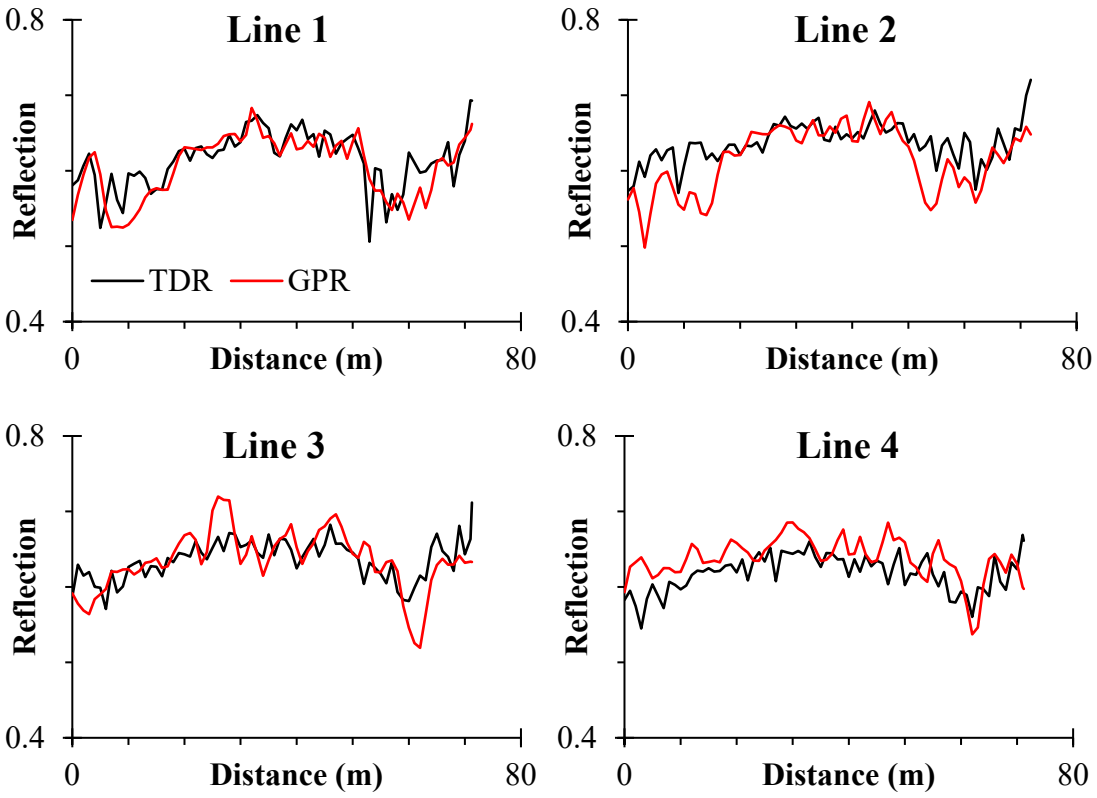

Fig. 12 Comparison of surface absolute reflectivity measured by UAV-GPR and TDR along four survey lines (Fig. 4a).

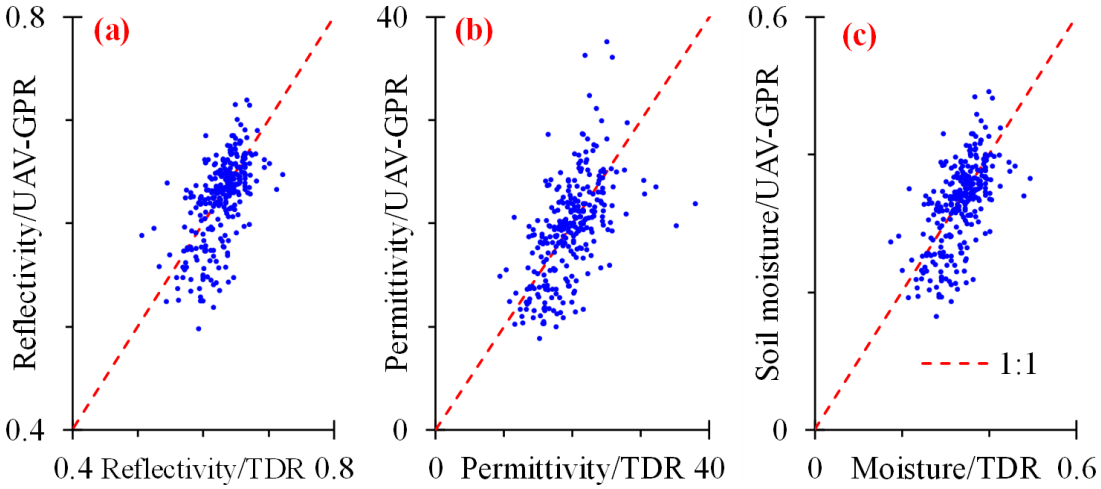

Fig. 13 UAV-GPR results versus TDR measurements in the grassland: (a) absolute reflectivity; (b) relative permittivity; (c) soil moisture. The red dashed line indicates a 1:1 match.

5. Discussion

5.1 Limitations of the multi-elevation GPR method

For the multi-elevation GPR method, the main assumption is that the transmitter and the reflection area of ground surface can be treated as point sources of radar signals. In general, two factors are necessary for the point source assumption: the size of transmitter is small, and the receiver is far away from the radar source.

For the GPR transmitter, the shape of antenna may affect the applicability of the multi-elevation GPR method. Because the bow-tie antenna (Fig. 1a) used in this study has a compact structure, it is suitable for the multi-elevation GPR method whatever the radar frequency (Fig. 5-7). In contrast, wire antennas belong to the family of one-dimension antenna, and can rarely be considered as a point source in a GPR system with a short separation distance between Tx and Rx [*Travassos et al.*, 2018]. Thus, their surface reflectivity estimation model should be different and more complex than the multi-elevation method. As shown in Fig. 14, we tested the Mala 100 MHz 'rough terrain antenna' (a non-point source antenna) using the UAV-GPR system. The reflected and air wave amplitude ratio clearly varies nonlinearly with the reciprocal of GPR height

(Fig. 14b), which is in disagreement with Eq. (9).

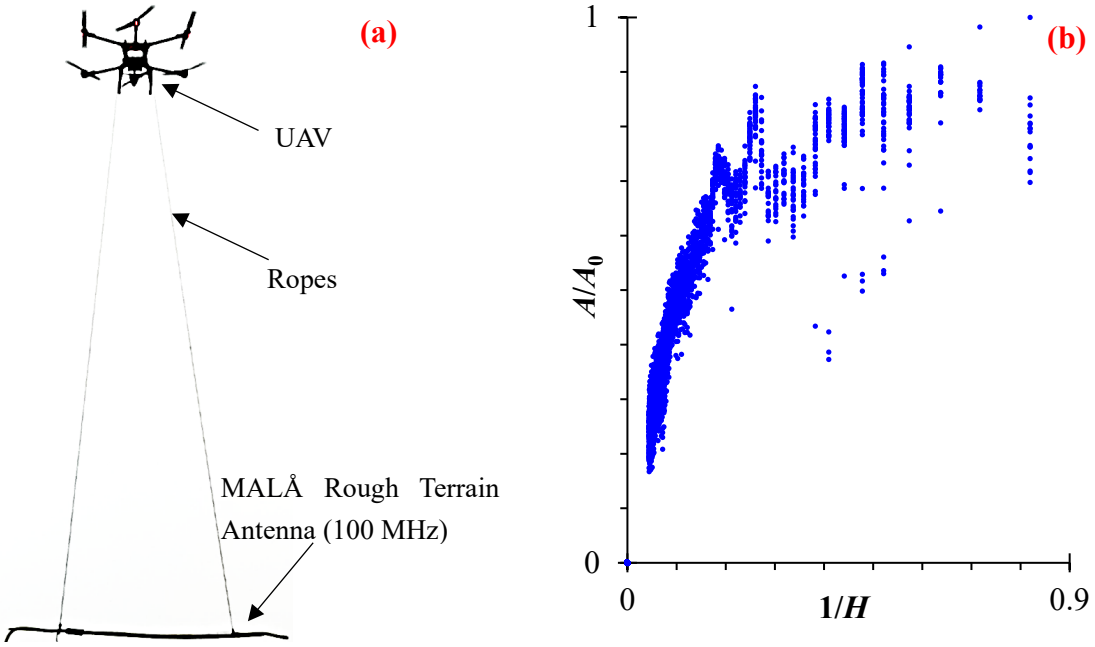

Fig. 14 Test of the Mala 100 MHz rough terrain (non-point source) antenna using the UAV-GPR method: (a) schematic of the UAV-GPR system; (b) the reflected and air wave amplitude ratio versus the reciprocal of GPR height, showing a clear non-linear response.

Because of the large area of the ground reflected radar source, the GPR height should be great enough to satisfy the point source assumption. Furthermore, in order to clearly separate the air and reflected waves, the GPR height should be greater than one half of incident wavelength. However, in practice, because an emitted radar signal of GPR usually includes two pulse waves [*Warren and Giannopoulos*, 2011], the GPR height should be greater than one wavelength e.g., 0.25 m for the 1.2 GHz antenna and 1.2 m for the 250 MHz antenna.

5.2 Effect of antenna frequency

As shown in the theoretical derivation processes (Eqs. (1) - (11)), the UAV-GPR method does not depend on the radar frequency. Although the antenna frequencies are different between the numerical simulation (1.2 GHz) and the field experiment (250 MHz), both

numerical and field experimental results confirm the theoretical findings as shown in Figs. 5-7.

In order to validate the effect of antenna frequency further, we tested other antenna frequencies (i.e., 2.3 and 1.2 GHz) above the water surface and the iron plate (i.e., of known reflectivity) using the point measurement mode. The investigation results are presented in Fig. 15. This figure shows that whatever the antenna frequency and the surface material are, the reflected and air wave amplitude ratios (A/A_0) are clearly directly proportional to the reciprocal values of GPR heights ($1/H$), verifying Eq. (9).

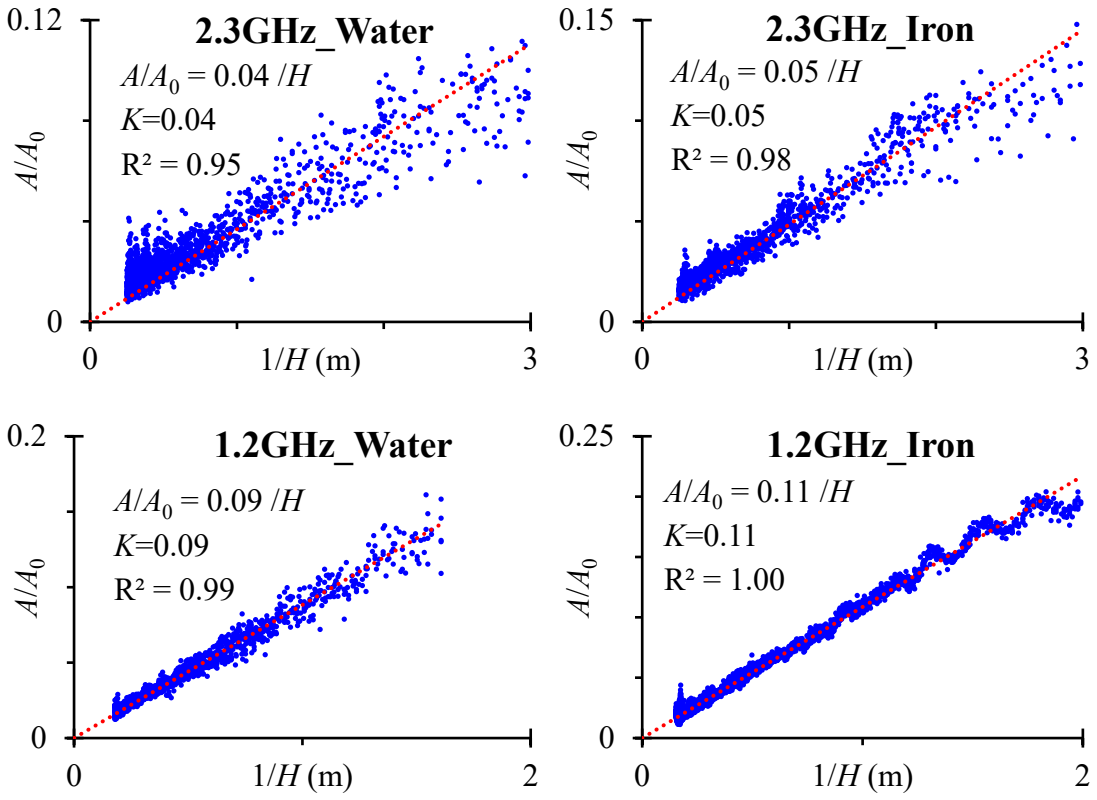

Fig. 15 The reflected and air wave amplitude ratio (A/A_0) versus the reciprocal of GPR height ($1/H$) for the water surface and the iron plate using the antenna frequencies of 2.3 and 1.2 GHz. The red dashed lines are the linear trend lines with an intercept of 0.

The slope coefficient (K) of linear trend line (in Fig. 15) versus the known surface

absolute reflectivity (|ξ|) for the 2.3 and 1.2 GHz antennas is presented in Fig. 16. This figure shows that for the both antennas, there is a significantly linear relationship between the slope value (K) and the surface reflectivity, which is in agreement with Eq. (10). Based on Eq. (16), we can calculate the shape factor (k) for 2.3 and 1.2 GHz antennas as 0.047 and 0.109 m, respectively. The k values are close to the Tx-Rx separation distance of 2.3 and 1.2 GHz antennas (i.e., 0.04 and 0.08 m, respectively), which is in line with Eq. (11). In summary, the UAV-GPR measurement method proposed in this study is appropriate for most radar frequencies. Note that for low frequency radar antennas (i.e., less than 250 MHz), as the soil electrical conductivity could interfere the surface reflection coefficient estimation (Eq. (19)) [*Wu and Lambot*, 2022], it is necessary to test the UAV-GPR method further.

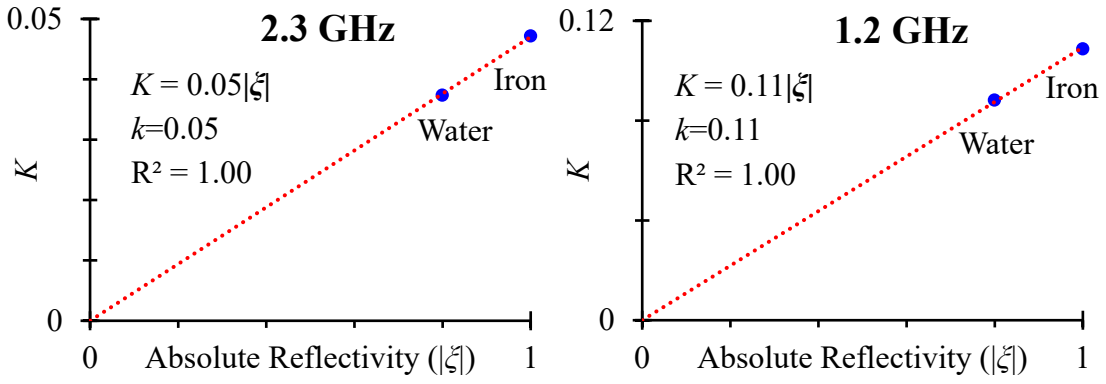

Fig. 16 The slope coefficient (K) of trend line (in Fig. 15) versus the surface absolute reflectivity (|ξ|) for the antenna frequencies of 2.3 and 1.2 GHz. The red dashed line is the linear trend line with the intercept of 0.

5.3 Significance of the multi-elevation GPR method

Comparison of the gprMax simulation results (Fig. 5a) and the field measurements (Fig. 6) reveals that there are obviously instrumental biases (i.e., the measurement errors of the reflected and air wave amplitudes and the antenna height (Fig. 1b)) of the GPR system, which will affect the accuracy of interpreted values (Fig. 9). As an example, the surface absolute reflectivity values of the iron plate at each record in Fig. 6 ("Iron plate") are calculated by Eq. (15) based on k (shape factor) = 0.33 m; the estimated

reflectivity values versus the corresponding antenna heights are shown in Fig. 17. This figure shows that the estimated reflectivity values (i.e., blue symbols) at different GPR heights randomly scatter around the true value (shown by the black line). Note that the absolute reflectivity values above 1 are not physically realistic but are a result of errors such as instrumental errors and the estimation error of *k*. The average relative error of reflectivity values at different GPR heights and the mean of the coefficient of variation are 8% and 11%, respectively.

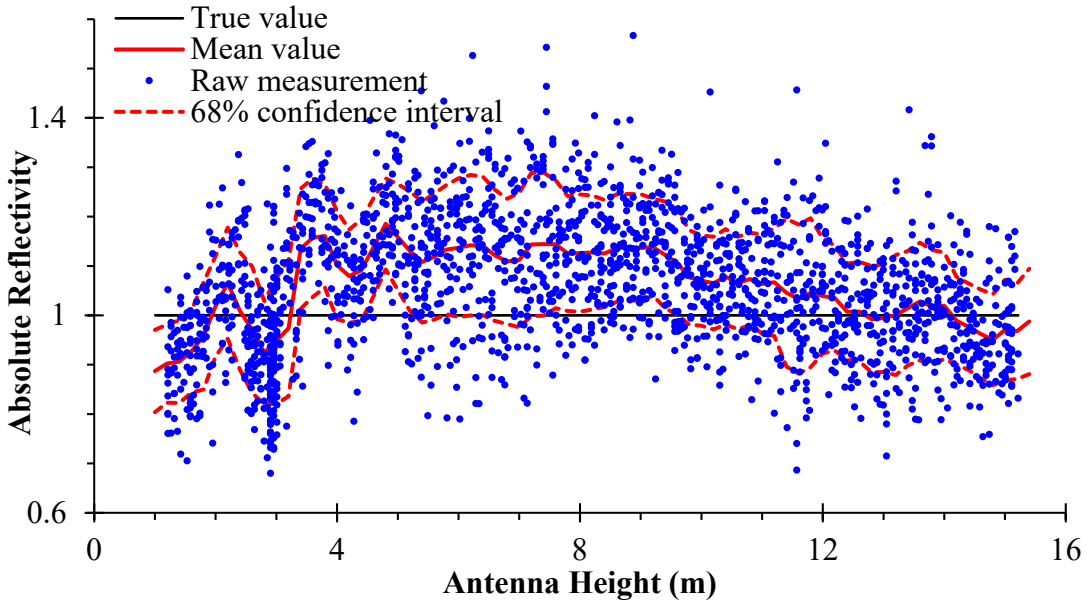

Fig. 17 The estimated surface absolute reflectivity values of iron plate at each record versus the corresponding antenna heights.

In general, a repeated measurement is an effective method to overcome many instrumental biases [*Schennach*, 2016]. However, as shown in Fig. 17, there may be systemic errors for the repeated GPR measurement at one elevation. Therefore, the multi-elevation GPR method (Eq. (15)) proposed in this study is required. The main advantage of the multi-elevation GPR approach is the use of the least squares approach to estimate the slope coefficient (*K*) value (Eq. (14)) used to determine the surface reflectivity value (Eq. (15)).

In order to evaluate the estimation accuracy of surface reflectivity, we compare the

estimated reflectivity values at a single antenna height with the TDR measurements in the grassland as shown in Fig. 18. This figure shows that the minimum reflectivity RMSE is located at 5.5 m. Therefore, 5.5 m seems to be the best antenna height for the single elevation investigation. However, the reflectivity RMSE of the multi-elevation method (shown by the red line in Fig. 18) is clearly less than that for all single elevation measurements. In other words, the multi-elevation method significantly improves the estimation accuracy of surface reflectivity.

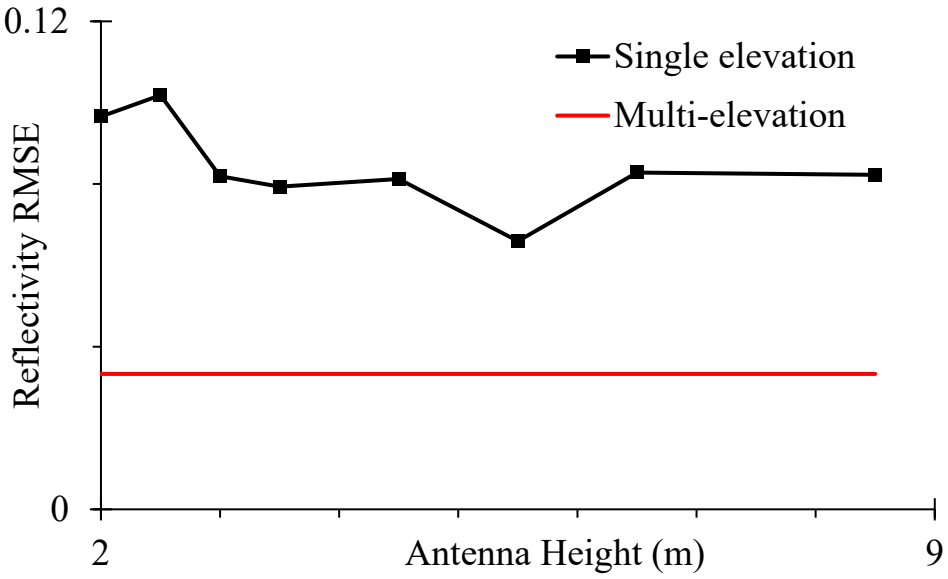

Fig. 18 The reflectivity mismatch (between GPR and TDR) of different single-elevation GPR investigations.

5.4 Resolution of the multi-elevation GPR method

The horizontal resolution (footprint) of a GPR system is usually characterized by the diameter of the first Fresnel zone. This zone is defined as the area of the reflecting surface that contributes to a single reflection, and can be treated as the footprint of GPR signals. The diameter (*FZD*) of the first Fresnel zone can be expressed as [*Huisman et al.*, 2003]:

$$FZD = \sqrt{\frac{\lambda^2}{4} + 2\lambda H}, \quad (21)$$

where λ is the radar wavelength of the Tx antenna.

The above equation shows the GPR resolution significantly increases with the antenna elevation and wavelength. The resolution is about 0.5, 0.7, 0.9 and 1.0 m for a 1.2 GHz antenna at an elevation of 0.5, 1.0, 1.5 and 2 m, respectively. And for a 250 MHz antenna, the resolutions are approximately 3.5, 4.9 and 6.0 m at an elevation of 5, 10 and 15 m, respectively.

In order to evaluate the effect of inhomogeneity of the soil on the slope coefficient estimation (K in Figs. 5a, 6 and 15) due to the GPR footprint, we re-built the soil stratum numerical model, where a square soil column (i.e., blue zone) with a relative permittivity of 2.0 and the side length of d is wrapped in the soil column (i.e., gray zone) with the permittivity of 5.4 and the side length of 0.8 m, as shown in Fig. 19a. In this study, the square column (cuboid) is chosen because it is a regular shape that can be more accurately discretized (by the cartesian regular grids used in the gprMax software) than an irregular shape (e.g., cylinder). Next, we ran the numerical model with different GPR heights (i.e., 0.2, 0.25, 0.35, and 0.45 m) for the side length (d) of 0.2 and 0.6 m, respectively.

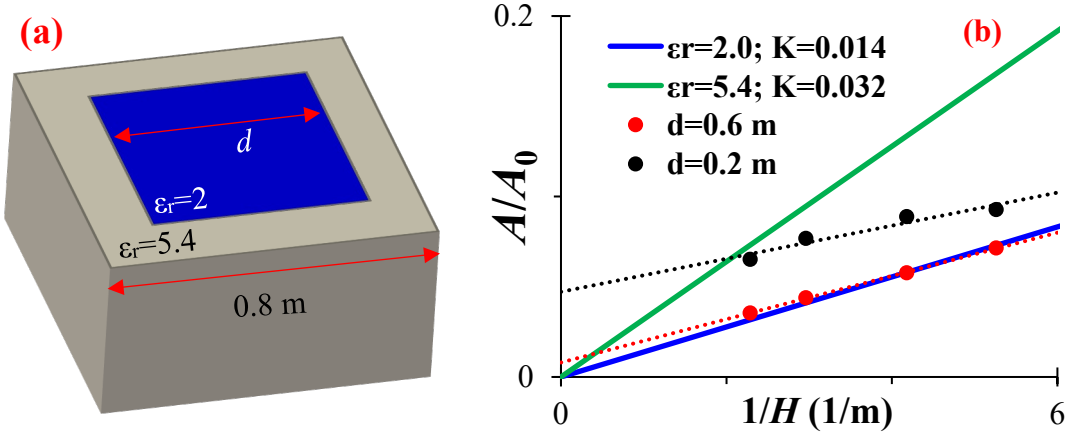

Fig. 19 The effect of the inhomogeneous materials of ground surface: (a) the soil stratum with wrap structure in the new numerical model; (b) the reflected and air wave amplitude ratio (A/A_0) versus the reciprocal of GPR height ($1/H$). The green and blue lines represent the linear relationships of A/A_0 and $1/H$ for the homogeneous soil stratum with the permittivity of 2.0 and 5.4, respectively. The black and red symbols

are the A/A_0 values at the corresponding GPR heights for the side length (d) of 0.2 and 0.6 m at the inner soil column, respectively.

The simulation results of gprMax software are presented in Fig. 19b. This figure shows the simulated results (symbols in Fig. 19b) all fall in the area between the blue and green lines (i.e., simulated results in the homogeneous soil stratum with ε_r=2.0 and 5.4, respectively, as shown in Fig. 5a), and as the GPR height increases, the symbols move closer to the green line, i.e., the properties of the outer zone in the model. In contrast, the symbols approach the blue line when the GPR height decreases, i.e., the values match better those of the inner zone in the model. These simulations reveal that the surface reflection (Eq. (10)) measured by the air-launched GPR possibly represents the integrated value of surface reflection in the GPR footprint area. And for the inhomogeneous medium, A/A_0 will be no longer directly proportional to the 1/H (Fig. 19b).

5.5 Effect of surface roughness and land cover on multi-elevation GPR method

Many studies have pointed out that surface roughness and land cover adverse to the soil moisture measurement by GPR [*Andre et al.*, 2019; *Jonard et al.*, 2012; *Lambot et al.*, 2006b]. Surface roughness can cause the diffuse reflections or scattering of EM waves, and lead to less energy being reflected in the specular direction. Furthermore, the land cover may shadow the ground surface. However, some studies have concluded that the low frequency EM waves with a large wavelength can reduce the adverse effects of these factors. For example, *Lambot et. al. [2006b]* showed that when the maximum height of the surface protuberances is less than one eighth of the GPR wavelength, the effect of surface roughness can be neglected. In other words, a surface is considered as rough if the surface protuberance is greater than one eighth of wavelength according to Rayleigh's criterion. Furthermore, the low frequency EM wave is also favorable to bypass obstacles (e.g., the individual stems or leaves of vegetations) according to the diffraction principle.

For a 250 MHz antenna, the wavelength reaches 1.2 m in a free space and the maximum protuberance height allowed in the ground surface can be 0.15 m. This threshold value is less than the drainage depth (i.e., 0.25 m) in the grassland (Fig. 4), and thus there are some abnormal investigation results (e.g., extremely low or high values) of the UAV-GPR method around the drainages as shown in Fig. 11. In contrast, for a 100 MHz antenna, the wavelength is 3.0 m and the maximum protuberance height allowed can reach 0.375 m. The large threshold value for the low frequency EM wave may indicate the multi-elevation GPR method is more suitable for application in areas with sparse or low height vegetation.

6. Conclusions

Based on the point source assumptions of a GPR transmitter antenna and ground reflections, we have developed a linear relationship between the reflected and air wave amplitude ratio and the reciprocal of GPR height, and verified the linear relationship by numerical simulation results using the gprMax software. We propose a multi-elevation UAV-GPR method (that uses a UAV to mount the GPR for spatial scanning investigation at different heights) to measure the surface reflectivity and estimate the soil moisture according to appropriate petrophysical relationships. Unlike previous air-launched GPR methods, the method purposed in this study removes the limitations of a steady transmitter power and a fixed GPR survey height, and the need for calibration of antenna transfer functions and geophysical inversion calculations, and thus is more convenient for field applications. We have tested the method at two field sites adjacent to the Yangtze River, and compared the measurement results with those inferred from TDR under the assumption of homogeneous medium in the first Fresnel zone. The results show that the measurement results of reflectivity, dielectric permittivity and soil moisture are all close to the TDR measurements. Compared with the single-elevation approach, the multi-elevation UAV-GPR method significantly improves the measurement accuracy. In the grassland with 8 antenna height investigations, the RMSE of surface reflectivity and soil moisture between GPR and TDR are 0.03 and 0.05 cm^3/cm^3, respectively.

In summary, the multi-elevation UAV-GPR may offer a useful method to measure the surface soil moisture, offering a higher resolution than remote sensing method and better working efficiency than conventional in-situ (e.g., TDR) methods. The horizontal resolution approximates that of the size of the GPR footprint, which offers a potentially useful intermediate measurement scale. For this method limitations mainly originate from the point source assumptions i.e., the compact structure of Tx antenna and the appropriate height of the Rx antenna. The multi-elevation method is an efficient approach to reduce the effect of instrumental errors (i.e., the measurement biases of the reflected and direct wave amplitudes and the antenna height) of GPR. Underlying surface conditions, e.g., surface roughness and land cover can affect the translation of measured reflectivity to soil moisture. This may limit application to areas of relatively uniform vegetation cover and benefit from locally derived permittivity - soil moisture relationships. Given the growing use of UAVs to support geophysical measurements, we expect to see further development and application of the method proposed here.

Acknowledgements

This research was funded by the Second Tibetan Plateau Scientific Expedition and Research Program (STEP; Ministry of Science and Technology, MOST; grant no. 2019QZKK0207-02), and the National Natural Science Foundation of China (Grant No. 42071039, 42030506, U21A2004 and 41971028). We are grateful to the Associate Editor and three anonymous reviewers for their valuable comments which helped to improve the manuscript.

Conflict of Interest

The authors declare no conflicts of interest relevant to this study.

Data Availability Statement

The data used in this paper is accessible at the website of https://doi.org/10.6084/m9.figshare.21892263.

References:

Algeo, J., et al. (2018), A comparison of ground-penetrating radar early-time signal approaches for mapping changes in shallow soil water content, *VADOSE ZONE J*, *17*(1), 1-11.

Anbazhagan, P., et al. (2020), Comparison of soil water content estimation equations using ground penetrating radar, *J HYDROL*, *588*, 125039.

Andre, F., et al. (2019), Accounting for Surface Roughness Scattering in the Characterization of Forest Litter with Ground-Penetrating Radar, *REMOTE SENS-BASEL*, *11*(7), 828.

Andreasen, M., et al. (2017), Status and perspectives on the cosmic-ray neutron method for soil moisture estimation and other environmental science applications, *VADOSE ZONE J*, *16*(8), 1-11.

Annan, A. P. (2005), Ground-penetrating radar, in *Near-Surface Geophysics, Invest. Geophys*., vol. 13, edited by D. K. Butler, chap. 11, pp. 357–438, Soc. of Explor. Geophys., Tulsa, Okla.

Ardekani, M. R. M. (2013), Off-and on-ground GPR techniques for field-scale soil moisture mapping, *GEODERMA*, *200*, 55-66.

Ardekani, M. R. M., and S. Lambot (2014), Full-wave calibration of time-and frequency-domain ground-penetrating radar in far-field conditions, *IEEE T GEOSCI REMOTE*, *52*(1), 664-678.

Babaeian, E., et al. (2019), Ground, proximal, and satellite remote sensing of soil moisture, *REV GEOPHYS*, *57*(2), 530-616.

Boopathi, N., et al. (2018), Towards soil moisture retrieval using tower-based P-band radiometer observations, in: *Proc. IEEE Int. Geosci. Remote Sens. Symp.*, 1407–1410.

Camillo, P., and T. J. Schmugge (1983), Estimating soil moisture storage in the root zone from surface measurements, *SOIL SCI*, *135*(4), 245-264.

Catapano, I., et al. (2021), Contactless ground penetrating radar imaging: State of the art, challenges, and microwave tomography-based data processing, *IEEE GEOSC REM SEN M*, *10*(1), 251-273.

Daniels, D. J. (2004), *Ground penetrating radar*, The Inst. of Electr. Eng., London.

Davis, J. L., and A. P. Annan (2002), Ground penetrating radar to measure soil water content. p. 446–463. In J.H. Dane and G.C. Topp (ed.) Methods of soil analysis. Part 4. SSSA Book Ser. 5. SSSA, Madison WI.

Dehem, M. (2020), Soil moisture mapping using a drone-borne Ground Penetrating Radar, Master: bioingenieur en sciences et technologies de lenvironnement thesis, Universite catholique de Louvain (UCL).

Diamanti, N., and A. P. Annan (2017), Air-launched and ground-coupled GPR data, paper presented at the 2017 11th European Conference on Antennas and Propagation (EUCAP), Paris, France, 19–24 March 2017; IEEE: New York, NY, USA, 2017; pp. 1694–1698.

Edemsky, D., et al. (2021), Airborne Ground Penetrating Radar, Field Test, *REMOTE SENS-BASEL*, *13*(4), 667.

Escorihuela, M. J., et al. (2010), Effective soil moisture sampling depth of L-band

radiometry: A case study, *REMOTE SENS ENVIRON*, *114*(5), 995-1001.
Huisman, J. A., et al. (2003), Measuring soil water content with ground penetrating radar: A review, *VADOSE ZONE J*, *2*(4), 476-491.
Jenssen, R. O. R., and S. K. Jacobsen (2021), Measurement of snow water equivalent using drone-mounted ultra-wide-band radar, *REMOTE SENS-BASEL*, *13*(13), 2610.
Jonard, F., et al. (2012), Accounting for soil surface roughness in the inversion of ultrawideband off-ground GPR signal for soil moisture retrieval, *GEOPHYSICS*, *77*(1), H1-H7.
Karthikeyan, L., et al. (2017a), Four decades of microwave satellite soil moisture observations: Part 1. A review of retrieval algorithms, *ADV WATER RESOUR*, *109*, 106-120.
Karthikeyan, L., et al. (2017b), Four decades of microwave satellite soil moisture observations: Part 2. Product validation and inter-satellite comparisons, *ADV WATER RESOUR*, *109*, 236-252.
Kaufmann, M. S., et al. (2020), Simultaneous multichannel multi-offset ground-penetrating radar measurements for soil characterization, *VADOSE ZONE J*, *19*(1), e20017.
Lakshmi, V., et al. (2013), Remote Sensing of Soil Moisture, *ISRN Soil Science*, *2013*, 424178.
Lambot, S., et al. (2004), Measuring the soil water content profile of a sandy soil with an off-ground monostatic ground penetrating radar, *VADOSE ZONE J*, *3*(4), 1063-1071.
Lambot, S., et al. (2006a), Analysis of air-launched ground-penetrating radar techniques to measure the soil surface water content, *WATER RESOUR RES*, *42*, W11403, doi:10.1029/2006WR005097.
Lambot, S., et al. (2006b), Effect of soil roughness on the inversion of off-ground monostatic GPR signal for noninvasive quantification of soil properties, *WATER RESOUR RES*, *42*, W03403, doi:10.1029/2005WR004416.
Linna, P., et al. (2022), Ground-Penetrating Radar-Mounted Drones in Agriculture, in *New Developments and Environmental Applications of Drones*, edited, pp. 139-156, Springer.
Liu, X., et al. (2019), Measurement of soil water content using ground-penetrating radar: a review of current methods, *INT J DIGIT EARTH*, *12*(1), 95-118.
Lopez, Y. A., et al. (2022), Unmanned Aerial Vehicle-Based Ground-Penetrating Radar Systems: A Review, *IEEE GEOSC REM SEN M,* 10(2), 66-86.
Lunt, I. A., et al. (2005), Soil moisture content estimation using ground-penetrating radar reflection data, *J HYDROL*, *307*(1-4), 254-269.
Mangel, A. R., et al. (2022), Drone applications in hydrogeophysics: Recent examples and a vision for the future, *The Leading Edge*, *41*(8), 540-547.
Minet, J., et al. (2010), Soil surface water content estimation by full-waveform GPR signal inversion in the presence of thin layers, *IEEE T GEOSCI REMOTE*, *48*(3), 1138-1150.
Minet, J., et al. (2012), Validation of ground penetrating radar full-waveform inversion

957 for field scale soil moisture mapping, *J HYDROL*, *424-425*, 112-123.
958 Muller, W. B. (2020), Semi-automatic determination of layer depth, permittivity and
959 moisture content for unbound granular pavements using multi-offset 3-D GPR,
960 *INT J PAVEMENT ENG*, *21*(10), 1281-1296.
961 Noviello, C., et al. (2022), An Overview on Down-Looking UAV-Based GPR Systems,
962 *Remote Sensing*, *14*(14), 3245.
963 Pritchard, H. D., et al. (2020), Towards Bedmap Himalayas: development of an
964 airborne ice-sounding radar for glacier thickness surveys in High-Mountain Asia,
965 *ANN GLACIOL*, *61*(81), 35-45.
966 Redman, J. D., et al. (2002), Field studies of GPR air launched surface reflectivity
967 measurements of soil water content, paper presented at Ninth International
968 Conference on Ground Penetrating Radar, International Society for Optics and
969 Photonics, 4758: 156-161.
970 Robinson, D. A., et al. (2008), Soil moisture measurement for ecological and
971 hydrological watershed-scale observatories: A review, *VADOSE ZONE J*, *7*(1),
972 358-389.
973 Schennach, S. M. (2016), Recent advances in the measurement error literature, *ANNU*
974 *REV ECON*, *8*, 341-377.
975 Shen, X., et al. (2020), Soil moisture retrieval depth of P-and L-band radiometry:
976 Predictions and observations, *IEEE T GEOSCI REMOTE*, *59*(8), 6814-6822.
977 Slater, L., and X. Comas (2009), Chapter 7 - The Contribution of Ground Penetrating
978 Radar to Water Resource Research, in *Ground Penetrating Radar Theory and*
979 *Applications*, edited by H. M. Jol, pp. 203-246, Elsevier, Amsterdam.
980 Stafford, J. V. (1988), Remote, non-contact and in-situ measurement of soil moisture
981 content: a review, *Journal of agricultural engineering research*, *41*(3), 151-172.
982 Topp, G. C., et al. (1980), Electromagnetic determination of soil water content:
983 Measurements in coaxial transmission lines, *WATER RESOUR RES*, *16*(3), 574-
984 582.
985 Travassos, X. L., et al. (2018), A review of ground penetrating radar antenna design
986 and optimization, *Journal of microwaves, optoelectronics and electromagnetic*
987 *applications*, *17*, 385-402.
988 Vereecken, H., et al. (2008), On the value of soil moisture measurements in vadose
989 zone hydrology: A review, *WATER RESOUR RES*, *44*, W00D06
990 doi:10.1029/2008WR006829.
991 Walter, C., et al. (2021), Characterizing electromagnetic interference signals for
992 unmanned aerial vehicle geophysical surveys, *GEOPHYSICS*, *86*(6), J21-J32.
993 Wang, J. R. (1987), Microwave emission from smooth bare fields and soil moisture
994 sampling depth, *IEEE T GEOSCI REMOTE*(5), 616-622.
995 Warren, C., and A. Giannopoulos (2011), Creating finite-difference time-domain
996 models of commercial ground-penetrating radar antennas using Taguchi's
997 optimization method, *GEOPHYSICS*, *76*, G37-G47.
998 Warren, C., et al. (2016), gprMax: Open source software to simulate electromagnetic
999 wave propagation for Ground Penetrating Radar, *COMPUT PHYS COMMUN*,
1000 *209*, 163-170.

Wu, K., et al. (2019), A new drone-borne GPR for soil moisture mapping, *REMOTE SENS ENVIRON*, *235*, 111456.

Wu, K., and S. Lambot (2022), Analysis of Low-Frequency Drone-Borne GPR for Root-Zone Soil Electrical Conductivity Characterization, *IEEE T GEOSCI REMOTE*, *60*, 1-13.

Ye, N., et al. (2020), Toward P-band passive microwave sensing of soil moisture, *IEEE GEOSCI REMOTE S*, *18*(3), 504-508.

Yueh, S., et al. (2019), Experimental demonstration of soil moisture remote sensing using P-band satellite signals of opportunity, *IEEE GEOSCI REMOTE S*, *17*(2), 207-211.

Zheng, D., et al. (2019), Sampling depth of L-band radiometer measurements of soil moisture and freeze-thaw dynamics on the Tibetan Plateau, *REMOTE SENS ENVIRON*, *226*, 16-25.

Figure Captions

Fig. 1 Air-launched ground penetrating radar: (a) principle; (b) characteristic parameters of received radar signals, where A and A_0 are the amplitudes of reflected and air waves, respectively; H is the antenna height; τ is the travel time difference between reflected and air waves and c is the radar velocity in air ($\approx 3\times10^8$ m/s).

Fig. 2 Multi-elevation GPR carried by UAV: (a) sketch of configuration; (b) prototype system in operation above a water surface (of known reflectivity).

Fig. 3 Location and geographic features of the riparian transect: (a) location; (b) aerial orthophoto; (c) digital surface model. Six red star symbols (P1 to P6) indicate locations where the point method was applied. The black asterisk marks the location of an observation well. The red line presents the route survey line, and the black circular symbols show the map scale.

Fig. 4 Geographic features of the grassland: (a) aerial orthophoto; (b) digital surface model. The water filled channel is demarked by a red line. The TDR survey lines are numbered as 1, 2, 3 and 4 sequentially from left to right.

Fig. 5 Numerical simulation results: (a) the reflected and air wave amplitude ratio (A/A_0) versus the reciprocal of GPR height ($1/H$); (b) the slope coefficient (K) of trend line in Fig. 5a versus the absolute reflectivity ($|\xi|$) of ground surface. The dashed lines are the linear trend lines with an intercept of 0. The symbols with different colors represent the different materials considered.

Fig. 6 The ratio of the reflected to air wave amplitudes (A/A_0) versus the reciprocal of GPR height ($1/H$) at the six test points, the river surface and the iron plate. The red dashed lines are the linear trend lines with an intercept of 0.

Fig. 7 The slope coefficient (K) of trend line between the reflected and air wave amplitude ratio and the reciprocal of GPR height (in Fig. 6) versus the absolute reflectivity ($|\xi|$) of ground surface. The red dashed line is the linear trend line with the intercept of 0.

Fig. 8 Normalized raw GPR signals received along the survey line at different antenna elevations: (a) 5 m; (b) 10 m; and (c) 15 m.

1045 **Fig. 9** Comparison of the UAV-GPR and TDR measurement results along the survey
1046 line: (a) absolute reflectivity; (b) relative permittivity; (c) soil moisture.
1047 **Fig. 10** UAV-GPR results versus TDR measurements: (a) absolute reflectivity; (b)
1048 relative permittivity; (c) soil moisture. The red dashed line indicates a 1:1 match.
1049 **Fig. 11** Measurement results of UAV-GPR in the grassland area: (a) surface absolute
1050 reflectivity at measurement points; (b) spatial distribution of surface absolute
1051 reflectivity interpolated by Kriging; (c) permittivity; (d) soil moisture.
1052 **Fig. 12** Comparison of surface absolute reflectivity measured by UAV-GPR and TDR
1053 along four survey lines (Fig. 4a).
1054 **Fig. 13** UAV-GPR results versus TDR measurements in the grassland: (a) absolute
1055 reflectivity; (b) relative permittivity; (c) soil moisture. The red dashed line
1056 indicates a 1:1 match.
1057 **Fig. 14** Test of the Mala 100 MHz rough terrain (non-point source) antenna using the
1058 UAV-GPR method: (a) schematic of the UAV-GPR system; (b) the reflected and
1059 air wave amplitude ratio versus the reciprocal of GPR height, showing a clear non-
1060 linear response.
1061 **Fig. 15** The reflected and air wave amplitude ratio (A/A_0) versus the reciprocal of GPR
1062 height ($1/H$) for the water surface and the iron plate using the antenna frequencies
1063 of 2.3 and 1.2 GHz. The red dashed lines are the linear trend lines with an intercept
1064 of 0.
1065 **Fig. 16** The slope coefficient (K) of trend line (in Fig. 15) versus the surface absolute
1066 reflectivity ($|\xi|$) for the antenna frequencies of 2.3 and 1.2 GHz. The red dashed
1067 line is the linear trend line with the intercept of 0.
1068 **Fig. 17** The estimated surface absolute reflectivity values of iron plate at each record
1069 versus the corresponding antenna heights.
1070 **Fig. 18** The reflectivity mismatch (between GPR and TDR) of different single-elevation
1071 GPR investigations.
1072 **Fig. 19** The effect of the inhomogeneous materials of ground surface: (a) the soil
1073 stratum with wrap structure in the new numerical model; (b) the reflected and air
1074 wave amplitude ratio (A/A_0) versus the reciprocal of GPR height ($1/H$). The green

and blue lines represent the linear relationships of A/A_0 and $1/H$ for the homogeneous soil stratum with the permittivity of 2.0 and 5.4, respectively. The black and red symbols are the A/A_0 values at the corresponding GPR heights for the side length (d) of 0.2 and 0.6 m at the inner soil column, respectively.